NOVA SCHOOL OF
SCIENCE & TECHNOLOGY

DEPARTAMENT OF
MATERIALS SCIENCE

Miguel Rodrigues Fialho

BSc in Materials Engineering Sciences

Computational Design of Colourful and Flexible Photonic-enhanced Solar Cells

MASTERS IN MATERIALS ENGINEERING

NOVA University Lisbon

March, 2023

DEPARTAMENT OF
MATERIALS SCIENCE

Computational Design of Colourful and Flexible Photonic-enhanced Solar Cells

Miguel Rodrigues Fialho

BSc in Materials Engineering Sciences

Adviser:	Prof. Manuel J. Mendes *Assistant Professor, NOVA University Lisbon*
Co-adviser:	Prof. Hugo Águas *Associate Professor, NOVA University Lisbon*

Examination Committee:

Chair:	Dr. Rui Igreja Associate Professor, *NOVA University Lisbon*
Rapporteur:	Dr. Kezheng Li Senior Researcher, University of York
Adviser:	Prof. Manuel J. Mendes *Assistant Professor, NOVA University Lisbon*
Member:	Prof. Hugo Águas *Associate Professor, NOVA University Lisbon*

MASTER IN MATERIALS ENGINEERING

NOVA University Lisbon
March 2023

Computational Design of Colourful and Flexible Photonic-enhanced Solar Cells

Dedicada ao meu irmão, Tomás.

ACKNOWLEDGMENTS

Antes de mais agradeço ao Professor Rodrigo Martins e à Professora Elvira Fortunato. Agradeço também a todos os professores e auxiliares do DCM e CENIMAT, que me acompanharam ao longo do meu percurso na FCT e me formaram como Mestre Engenheiro.

De seguida quero agradecer ao meu orientador, Professor Manuel Mendes e ao meu co-orientador, Professor Hugo Águas, pelo tema de tese que me propuseram. Até à data foi inegavelmente o projeto mais ambicioso e gratificante no qual já tive o privilégio de participar. Agradeço-lhes a orientação e, ademais, agradeço-lhes pela atenção e tempo disponibilizado na minha integração na equipa de investigação do CEMOP, à qual extendo a minha gratidão.

No CEMOP quero agradecer especialmente à Jenny Boane pelos dados da reflexão indispensáveis à justificação dos meus métodos, ao António Vicente pelos conselhos que me deu para as apresentações, e ao Ivan Santos pela boa vontade com que me deixou interromper o trabalho dele para ver se as simulações ainda estavam a correr. O maior agradecimento devo-o, sem dúvida, ao Mestre Miguel Alexandre, sem o qual esta tese não teria sido possível. Agradeço-lhe pelas inúmeras revisões aos meus gráficos e rascunhos amadorísticos, por me incentivar a querer aprender a programar "como deve de ser" e sobretudo pela amabilidade e diligência com que sempre me respondeu às dúvidas – por mais básicas que estas fossem.

Ainda no contexto da faculdade, quero agradecer aos meus colegas de curso, Alex, António, Carolina, Camecelha, Martins, Gonçalo, Jorge, Manel, Ricardo, Rita, Xavi e Vitor, por ordem alfabética para não se brigarem. O curso não se faz sozinho. Eu fi-lo bem acompanhado.

Agradeço ao Luis Monteiro por me ensinar a olhar para o absurdo e pensar: *"lightweight!"*.

Agradeço à Weatherlight, tripulação e co-capitães, pelas tardes de sábado bem passadas.

Agradeço à minha Maria, por tudo. Aos meus amigos de infância, Bsy, Bolo, Cavaco, David, Rui, Velha, Bagoso, Rita, Fiona e Duarte agradeço por ordem de chegada (acho eu).

Agradeço à minha familia, especialmente ao meu irmão, de quem eu me orgulho tanto.

"Truly the light is sweet, and a pleasant thing it is for the eyes to behold the sun."

Ecclesiastes 11:7 (KJV)

ABSTRACT

The need for coloured solar cells is particularly relevant to the adoption of photovoltaic devices in building-integrated photovoltaics. This thesis describes the process by which perovskite-based thin-film ($MAPbI_3$) solar cells (PSCs) were optimised to tune colour without compromising flexibility whilst increasing short-circuit current density (J_{SC}). Solar cells containing antireflective front coatings of planar, nanopillar and cross-grating geometries are simulated in a three-dimensional space by the Finite Differences in Time Domain (FDTD) numerical method using Ansys Lumerical software. The main outcomes of the numerical simulations are the optical photocurrent and the overall reflection, which is converted into colour using the CIE 1931 Colour-matching functions for standardised observers. Two Figures of Merit were developed, based on the optical photocurrent and the Euclidian distance between the simulated and desired colour. The best of the two FoMs is maximized via particle swarm optimization algorithm, by variation of geometrical properties of the front coverings and intrinsic ITO and Spiro-OMeTAD layer thicknesses. Through analytical elimination of redundant variables and successive restrictions in parameter ranges, the optimal geometrical parameters for flexible thin-film photonically-enhanced PSCs coloured red, green, or pink are obtained for increases in J_{SC} upwards of 10.7%, and a versatile methodology is posited for future optimizations.

Keywords: Photonics, Solar Cells, Perovskite, Structural Colour, BIPV, Thin-film

RESUMO

A necessidade de células solares coloridas é particularmente relevante à adoção de dispositivos fotovoltaicos em equipamentos incorporados em facetas arquitetónicas. Esta dissertação descreve o processo pelo qual células solares de filme-fino à base de Perovskite (MAPbI3) foram otimizadas para ajustar a cor sem prejudicar a flexibilidade e aumentando a densidade de corrente. Células solares contendo revestimentos frontais antirreflexo de geometrias planares, nano-pilares e grelhas cruzadas são simuladas num espaço tridimensional pelo método numérico de Diferenças Finitas no Domínio do Tempo com o software *Ansys Lumerical*. Os principais resultados das simulações numéricas são a foto-corrente e a reflexão global, que é convertida em cor utilizando as funções de correspondência do CIE 1931 para observadores normalizados. Desenvolveram-se duas figuras de mérito, com base na foto-corrente e na distância Euclidiana entre a cor simulada e a cor desejada. A melhor figura foi maximizada por otimização *Particle Swarm* ao variar as geometrias das estruturas fotónicas frontais e das camadas intrínsecas de ITO e Spiro-OMeTAD. Após eliminar variáveis redundantes e restringir os intervalos de otimização, obtiveram-se geometrias ótimas para obtenção de estruturas coloridas vermelhas, verdes e rosa acrescendo aumentos de corrente superiores a 10.7% com o desenvolver de uma metodologia versátil aplicável a futuras otimizações.

Palavras-chave: Fotónica, Células Solares, Perovskite, Cor Estrutural, BIPV, Filme-fino

CONTENTS

LIST OF FIGURES

LIST OF TABLES

GLOSSARY

CIE Method	Method of mapping reflection spectra to a set tristimulus values from which colour can be extrapolated.
gbest	Global best value for all the particles in a Particle Swarm Optimization.
Green	Specifically refers to hexcode #00FF00 or RGB (0, 255, 0).
Light-trapping	Structural property defined by an increase in optical path length primarily via light scattering and refraction effects.
Particle Swarm Optimization	Stochastic optimization algorithm that simulates the social behaviour of swarms by iteratively updating candidate solutions based on their fitness, allowing for the efficient search of high-dimensional solution spaces.
Perovskite	Singular form refers to $MAPbI_3$ unless stated otherwise.
Photonic	Pertaining to photon-level interactions.
Pink	Specifically refers to hexcode #FF69B4 or RGB (255, 105, 180) .
Pitch	Distance between the starting points of neighbouring cell units as a multiple of their respective width value.
Red	Specifically refers to hexcode #FF0000 or RGB (255, 0, 0).
Seed	Base value from which *"randomness"* is generated.
Spiro	Shortened version of Spiro-OmeTAD.
Structural Colour	Colour which is produced via light interference on a structural level, rather than through dyes or pigmentations.
Thin-Film	Films with thicknesses ranging from 10^{-9} meters to 10^{-5} meters.

ACRONYMS

3D	Three-dimensional
AM	Air Mass
API	Application Programming Interface
ARC	Anti-reflection Coating
AST	The American Society for Testing and Materials
BIPV	Building Integrated Photovoltaic
CAD	Computer-aided Design
CIE	Commission Internationale de l'éclairage (International Commission on Illumination)
ETL	Electron-Transport Layer
FDTD	Finite-Difference Time-Domain
FoM	Figure of Merit
HTL	Hole-transport Layer
LT	Light-trapping
PML	Perfectly Matched Layer
PSC	Perovksite Solar Cell
PSO	Particle Swarm Optimization
PV	Photovoltaic

RMS	Root-mean-squared
SC	Solar Cell
TCO	Transparent Conductive Oxide
TFSC	Thin-film Solar Cell
UV	Ultraviolet

SYMBOLS

A	Absorption per unit of volume
eV	Electronvolt
GW	Gigawatt
Jsc	Short-circuit Current Density
k	Imaginary Part of the Refractive Index, also called Extinction Coefficient
K	Kelvin degrees
mA	Milliampere
n	Real Part of the Refractive Index
nm	Nanometre
t	Tolerance factor
TW	Terawatt
λ	Wavelength
ω	Angular Frequency

1 INTRODUCTION

1.1 Market Overview

The field of photovoltaic (PV) technology has made significant progress in recent years. Bloomberg Intelligence's Global Solar Energy 2023 Outlook report predicts a substantial increase in demand for solar energy, with a projected growth of 20-30% in 2023 [1]. In addition, Trendforce estimates that 350.6 GW of PV systems could be installed this year, representing a 53.4% increase from 2022 [2]. The positive market outlook is due to recent market and technological advancements and solar's cost leadership, which has been steadily improving and out-competing fossil fuels and nuclear in any unsubsidized investment case [3].

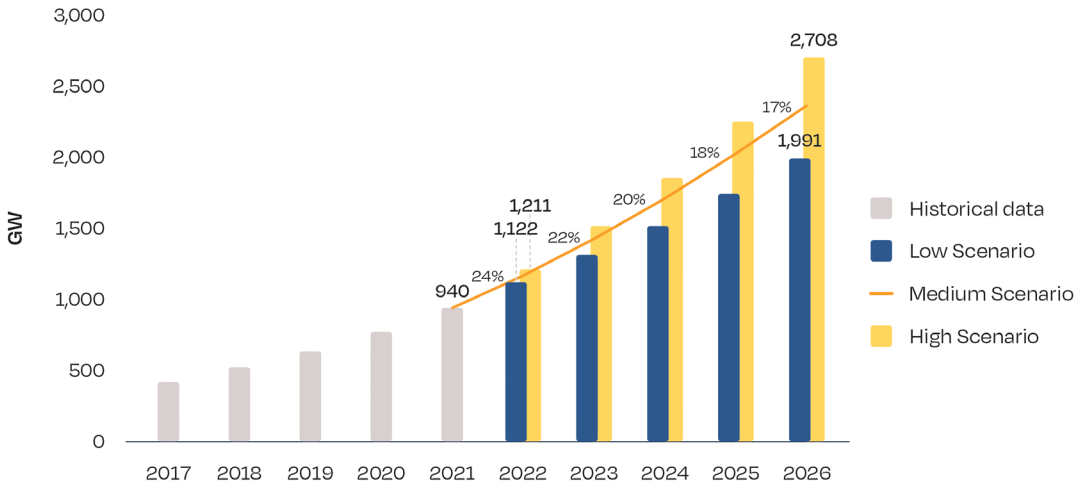

Figure 1.1 – Global solar market forecast in 2017-2026. Source: Solar Power Europe [3]

The solar energy sector's strong upward trajectory is evident in recent analyses predicting that worldwide solar capacity will exceed 2 TW by the end of 2025 [3]. Solar energy is also projected to surpass coal power by 2027 [1], indicating the potential to significantly alter the global energy landscape.

1.2 Building Integrated Photovoltaics

The market for solar cells (SCs) can be further expanded upon by exploring novel implementations, such as their integration in buildings, where they could also serve as a safeguard from weather-induced degradation [4]. In the EU, buildings are collectively responsible for 40% of the total energy consumption [5], [6]. Building Integrated Photovoltaics (BIPV) could alleviate this energetic burden while also compensating for it by turning the façades of modern buildings into solar farms, all the while satisfying the base requirements imposed on traditional building envelopes [7]–[9]. This building-generated energy would be fundamental to minimising strain on the power grid, which is often a limiting factor for non-on-demand energy sources, like most renewables[10]. These systems can integrate with the power grid or stand alone. Moreover, BIPV can be integrated into many facets of architectural design in roofs, façades, blinds, shutters, decorative features, shading or railings, [7], [11], [12] fenestration elements [13] or fences [14].

There are several intrinsic prerequisites for the application of a material as a building envelope, namely its fire safety, mechanical resistance, durability, and hydro and geothermal performance [7]. Additionally, the inhomogeneity of solar irradiance poses yet another challenge by being highly dependent on the direction that the façades of the buildings face [7]. This is further complicated by the fact that a BIPV installation with a fully vertical orientation only outputs roughly 75% of the energy a system with a 20-degree tilt angle would produce under optimal conditions [12],[13]; this downside may be offset by tilting the systems relative to the façade, forsaking aesthetics[12]. Furthermore, partial shading from surrounding buildings is also worth considering, especially in megacities [8]. Shading from snow or dust can also stunt the performance of these modules and potentially lead to hotspot defects, though this can be mitigated with self-cleaning (hydrophobic) coatings[15]–[17]. Active and/or passive cooling may also be included to prevent overheating [17], [18].

Despite these hurdles, there has been a substantial increase in both the market and the developers' interest in BIPV, which brought about a reduction in the costs associated with its installation and a subsequent increase in its viability [13]. Nevertheless, the global BIPV market still has considerable room for expansion [12], [13]. Gholami et al. 2020 found that, given an investment discount rate of 5% in Europe, BIPV systems would be capable of fully reimbursing the installation and maintenance expenditures for all installations not facing

northwards [8]. From a generalized stakeholder's perspective, current BIPV systems are already economically favourable [19].

1.3 Coloured Photovoltaics

For BIPV to become a staple of modern architecture, beyond its remarkable potential to satisfy the energetic demands of the current ever-growing number of urban sites while being financially sound, certain aesthetic requirements must be met, lest these potential technologies be shunned by architects and the public alike [14], [19]. In this sense, colour is one of the most relevant factors limiting the adoption of these technologies [10]. These aesthetic requirements are particularly pertinent regarding the integration of these systems when considering the preservation of architectural cultural heritage and natural landscapes [10], [11], where the typical dark colours associated with photovoltaics would not fit.

The main drawback associated with coloured PVs, aside from the logistics behind its conception, is the fact that the colour exhibited i.e. the light reflected is in essence, intentionally wasted potential photocurrent [10], [14]. M. Chivelet et. al. quantifies photocurrent losses of between 7-50% based on the colour being reflected [7]. An upside of these reflection losses is the diminished need for cooling resulting from decreased absorption [14]. In the present literature, there are several different methods of obtaining colour in SCs, some of the more relevant being: anti-reflection coatings (ARC), coloured or semi-transparent PV-active layers, solar filters inserted within or on top of the base cell layers, coloured polymeric encapsulants and customized glass fronts containing coloured dot patterns [11], [12], [17]. The work described herein uses structural colours obtained by light-wave interference, which can be customized by tuning the different geometrical structural parameters defining the front coating of a perovskite solar cell (PSC). One key advantage that structural colour has over pigments is the fact it is less likely to sun-bleach or fade over the device's lifespan [14].

1.4 Perovskite Solar Cells

In 2009 Kojima et. al. reported a 3.8% efficiency conversion rate for a very short-lived and yet promising perovskite nanocrystal [20] and since then more publications are published each year, in a trend set to last for the foreseeable future [21], [22] as the current record efficiency reached 25.7% in 2023 [23], [24]. Their attractiveness to researchers and investors comes from their excellent optoelectronic properties, notably their light absorption, charge carrier

mobility, and low exciton binding energy [20], [22]. Some benefits of PSCs include high carrier lifetime, low surface bandgap and tuneable bandgaps [22], [28]. Its fabrication is highly scalable [27], comparatively simple, cost-effective [26] and viable on flexible substrates [22].

Perovskites are characterized by an ABX_3 organometallic-halide chemical formula, where A is a monovalent organic cation like methylammonium (MA+) or formadinium (FA^+), B is a divalent metal cation such as Pb^{2+} or Sn^{2+} and X is a 17th group halogen like I^- Br^- or Cl^- [22], [25], [26], [28]. These three constituents may be proportioned in terms of their stoichiometry to tune the bandgap of the perovskite, which would optimally fall within the 1.2-1.62 eV range for most photovoltaic applications [26]. $MAPbI_3$, the most commonly used perovskite - the one herein explored– has direct a bandgap of 1.55eV [22], a well-defined peak in absorption coefficient for incident energy levels immediately past its bandgap value [26].

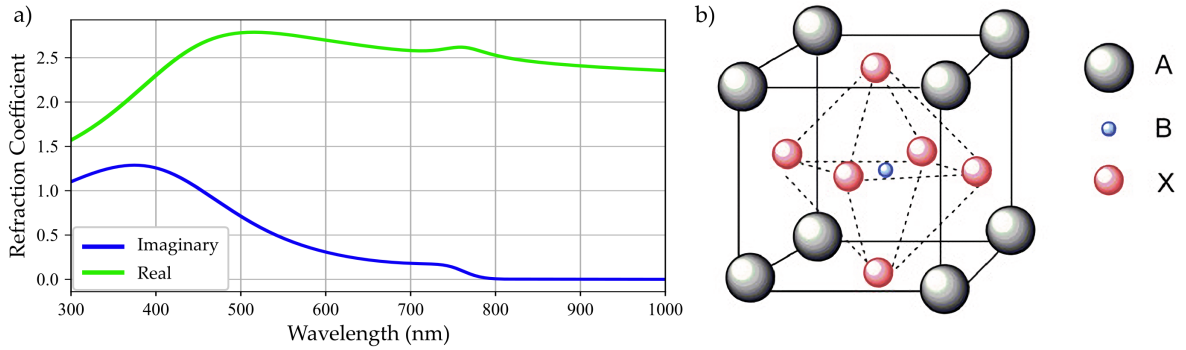

Figure 1.2 – $MAPbI_3$ Perovskite real and imaginary part refractive index (a) and ABX3 crystalline structure (b).

The main drawback of PSCs is their stability when exposed to light, heat and moisture, especially when compared to silicon-based cells [29]. The stability of PSCs is paramount in BPV applications, particularly in the case of lead-based perovskites. The negative environmental and health impacts of lead have been well documented for centuries, thus proper encapsulation must not only shield the PSC from heat, UV radiation and moisture, but also effectively prevent the leakage of harmful by-products [12], [27]. There have been multiple reports of cells lasting longer than 1000 h while keeping energy generation above 80% of its initial value [30], [31] and recent work done by Zhao et. al. describes the process by which specific PSCs were designed to last over 5 years operating continuously at 35°C [32], but these records are still far below the standard 25-year warranty of typical silicon modules [25], [33].

1.5 Photonic-enhanced Thin-film Solar Cells

There are considerable benefits associated with the reduction in the thickness. One such benefit is the reduction in the amount of material used in the production of these devices. This

reduction is particularly relevant when considering scarcer or toxic materials, such as the lead in the absorber layer of PSCs [34]–[36]. In theory, this would also lead to a reduction in manufacturing costs, but this is offset by the added cost and complexity of the resulting structures [37]. Additionally, reducing thicknesses would also mitigate the risks associated with growing material demands or the market volatility of the Ag used in the cells studied herein [38], [39]. Provided the cell is not limited by surface recombination, thickness reduction diminishes bulk recombination and increases open circuit voltages, correlating with higher efficiency[40], [41]. Granted the mean charge diffusion length remains unaltered, this increase in efficiency is compounded by a reduction in carrier transport loss, especially in amorphous materials [41]. Thin-film solar cells (TFSCs) are also more industrially scalable as they can be fabricated via roll-to-roll processing [36]. Regrettably, as of 2021, there were still no viable designs for bendable SCs [42]. Lowering the thickness of these designs would allow for greater flexibility of the SCs, at the cost of reducing their light absorption — a downside which is mitigated by the implementation of light-trapping (LT) photonic structures [43].

Photonic structures often make simultaneous use of four light management techniques, namely light in-coupling, scattering, internal reflectance and geometric index matching [43]. These structures can be designed to avoid negatively impacting the flexibility of the cells and may be employed in the back, front, or both sides of the absorber layer [44] which could also be nanostructured itself [36],[40]. Refractive index mismatch between media causes reflection losses [36], [45]. When considering photonic structures applied to the front of the cell, the complex refractive index of an ideal LT coating would possess a null imaginary part and a real part matching the absorber layer [34]. An increase in the real part of the reflective index of a photonic structure leads to a pronounced field scattering effect from angular refraction [40]. Depending on the shape of the structure, a geometrical refractive index gradient is achieved to counteract the mismatch between the cell and the air by gradually increasing the volume of photonic material interacting with the light [45]. One of the ways in which of photonic structures benefit TFSCs has to do with the mitigation of the effect that the angle of incidence has on the cell efficiency. Conversion efficiency is maximized when light is directly projected upon the surface of the cell (at a 0-degree angle) and minimized when this angle reaches 90° [42]. These structures can allow the cell to produce an optical response for incidence angles as high as 70° [46]. This effect is particularly relevant for BIPV and wearable devices, as these devices most likely are not directly facing the sun and solar tracking is unfeasible [47], [35].

2
MATERIALS AND METHODS

2.1 Simulation Methods and Yields

This work uses the Finite Differences Time Domain (FDTD) method to accurately solve Maxwell's equations and thus study light-matter interaction in solar cells. The FDTD method directly approximates Maxwell's equations via finite differences approximation [48], [49], which not only allows for extreme versatility in terms of the allowed simulation geometries, but also the optical models for the individual materials [48]. FDTD is an indispensable tool which facilitates the accurate prediction of the behaviour of these theoretical solar cells. The software chosen to apply this method is Ansys Lumerical FDTD Solutions. This software incorporates a 3D CAD environment which will be used to model the cells. Additionally, Lumerical is also viable for Python integration via a prebuilt Application Programming Interface (API). It is through this API that these simulations will be tuned and executed. The resulting data is parsed, interpreted, and stored within the Python environment.

The simulation yields needed for this work are the generated photocurrent density (J_{sc}) and the reflection spectrum. The former is fundamental to determining the colour of the device while the latter defines the amount of light absorbed by the cell that can be directly converted into an electrical current, given by Equation 1 for the AST G-173 global solar irradiance.

$$J_{sc} = \int A(\omega) AM_{1.5G} d\omega \quad (1)$$

2.2 Colour Processing Methods

The reflected power spectrum determines the appearance characteristics of the reflected light, namely its hue, lightness, and saturation [50]. Hue is the measurement by which the observer perceives the base colour of an object as being red, green, blue, pink, etc. [50]. Lightness

determines how bright the perceived colour is, and is used to distinguish between different shades of the same colour; regardless of its base hue [50]. Two objects are considered to be of equal lightness if they reflect equal amounts of light [51]. Saturation, is the degree of separation between a colour and its grey counterpart [51]. Perception of colour, especially regarding lightness, depends on the observer's macular pigmentation [52], [53]. Additionally, the lightness of the reflected colour is inversely proportional to the overall absorption of incident light. Accounting for this, it was deemed preferable to, at least in the earlier stages of development, isolate the optimization of the colour of a simulated solar cell in terms of hue and saturation. Not only would this be the most relevant factor to determine whether a certain colour was being approximated, but it would also make it easier for a human observer to distinguish between different iterations, since all the colours would be portrayed at maximum lightness and not as multiple different shades of the same dark tones.

The colour of the simulated solar cell can be extrapolated from the power spectrum obtained by the multiplication of its reflection spectrum and the simulated solar power spectrum built into Lumerical [54]. The reflected hue of the device can be determined from the CIE Colour Matching Functions. These functions match the reflection power spectrum to a set of three tristimulus values each of which is analogous to one of the three cone cells with which the human eye perceives the attributes of the colour [55]. These adimensional tristimulus values, denoted by X, Y and Z, are given by the functions plotted in Figure 2.1.

$$X = \int P(\lambda)x(\lambda)\,d\lambda$$
$$Y = \int P(\lambda)y(\lambda)\,d\lambda$$
$$Z = \int P(\lambda)z(\lambda)\,d\lambda$$

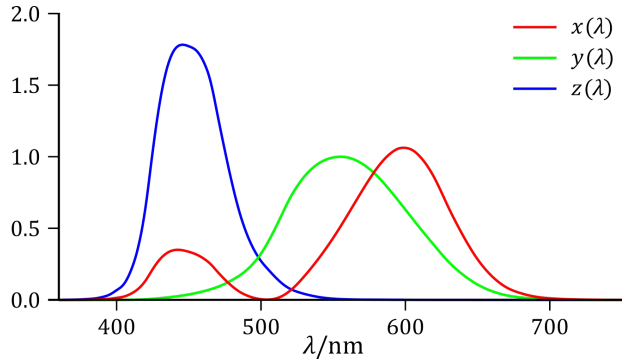

Figure 2.1 – Set of functions from which the adimensional tristimulus values are calculated and the graphical representation of the CIE standardized values as a function of the reflected wavelength (λ) in nanometers.

These tristimulus values can be normalized by the division of their sum to obtain only the information pertaining to chromaticity, that is its hue and saturation. In doing so the colour can be mapped to its x and y variables at the cost of its lightness as given by the following equations [55], [56].

$$x = \frac{X}{X+Y+Z},\ y = \frac{Y}{X+Y+Z},\ z = \frac{Z}{X+Y+Z} = 1 - x - y \qquad (2, 3, 4)$$

The values calculated for x and y can be converted to RGB values by multiplying the (x, y, z) vector by the inverse matrix of the three primary chromaticities, which have been tabulated for all the wavelengths between 380 and 780 nm for a 2° visual angle by the International Organization for Standardization. [57]

$$\begin{pmatrix} x_r & x_y & x_b \\ y_r & y_g & y_b \\ z_r & z_g & z_b \end{pmatrix}^{-1} \begin{pmatrix} x \\ y \\ 1-x-y \end{pmatrix} = \begin{pmatrix} r \\ g \\ b \end{pmatrix} \qquad (5)$$

The three standardized primary colours' tristimulus values used in the colour-matching function were obtained through experimental investigations by WD Wright using monochromatic wavelengths of 700 nm, 546.1 nm and 435.8 nm for the red, green, and blue primaries, respectively [58].

To serve as the definition of the colour white, the chosen standardized illuminant was the CIE D65 as it closely represents average daylight with a colour temperature of 6504 K. [53], [54] If one of these pairs of (x, y) coordinates were to fall outside of the RGB gamut the values of its components are equally raised until they fit the RGB space [55].

2.3 Figure of Merit

RGB is an additive colour model, meaning that each colour is described as the additive mixture of red, green and blue lights [53]. Colours defined in RGB values are more similar the closer their RGB values are. If we place a colour in a three-dimensional vectorial space where its cartesian coordinates are defined directly by its RGB values we can determine the distance between two colours by its Euclidean Distance, given by Equation 6:

$$\text{Colour Distance} = \sqrt{(r-R)^2 + (g-G)^2 + (b-B)^2} \qquad (6)$$

Where (r, g, b) and (R, G, B) are the RGB values corresponding to each of the two colours. Using these results two Figures of Merit (FoM) with which to compare the performance of different structures are theorized, as per equations 7 and 8.

$$\text{Original FoM} = \frac{Jsc}{Colour\ Distance} \quad \text{Root FoM} = \frac{Jsc}{\sqrt{Colour\ Distance}} \qquad (7, 8)$$

These FoMs differ in the emphasis put on minimizing the Colour Distance. In theory, the Original FoM should place equal importance in maximizing the J_{SC} and minimizing the Colour Distance, whereas the Root FoM should prioritize maximizing the J_{SC} over minimizing the Colour Distance given that the intent is to reach a colour as similar (and thusly as close) as possible to the intended colour, both FoM are inversely proportional to the colour distance and directly proportional to the generated current density. Meaning that the higher the FoM value the higher the relative performance of the solar cell in terms of its ability to generate photocurrent without compromising its colour.

2.4 Particle Swarm Optimization

Particle Swarm Optimization (PSO) is a stochastic, iterative, population-based multi-parameter optimization algorithm [59]. This "smart-search" type optimization technique attempts to find the best set of parameters as opposed to solving for an optimal continuous function [60]. PSO handles a set number of particles, each with a randomized starting position and velocity vectors. The coordinates of each particle represent the optimized parameter values in a finite space. Upon the beginning of an iteration, each particle records the response of the function for its corresponding parameters. This information is then shared among the population, so that the particles may converge in clusters where the best response is being recorded [59], [60]. This convergence happens by adjusting the velocity vector for each particle and redirecting towards the current best. The new velocity is calculated considering three factors, the inertia weight, the social learning factor, and the cognitive learning factor, the first of which dictates how much of the particle's momentum is conserved while the remaining two factors regulate the pull towards the global and individual current best, respectively [61]. This methodology is summarized in Figure 2.2. PSO has been used in the computational design of photonic structures [62], [63]. Most pertinently, this method is suited to complex problems involving non-linearity, multiple optimization parameters and local optima [61]. This method is easy to implement [64]and time-efficient, especially in comparison with the parameter sweeping method whose complexity rises exponentially with the number of optimization variables.

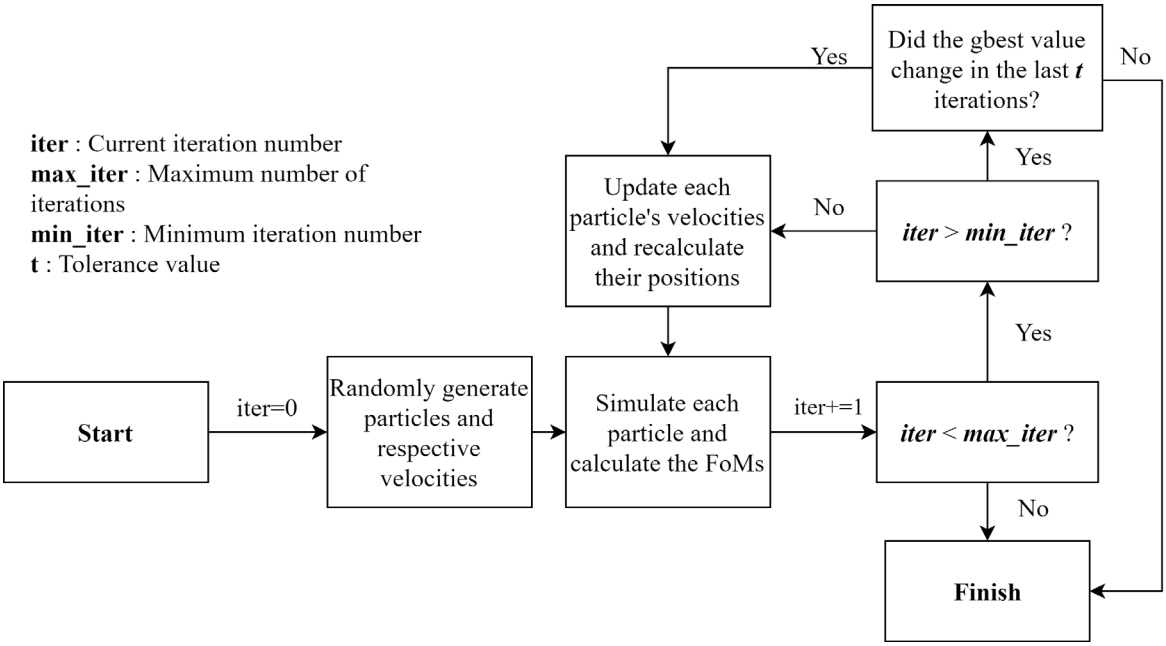

Figure 2.2 – Flowchart description of the basic operating principles behind the particle swarm optimization method.

2.5 Solar Cell Structures

Typical PSCs are composed of a metal cathode serving as the back contact, a hole transport layer (HTL) to lead the holes into the contact, an absorber layer where photocurrent is generated, an electron transport layer (ETL) to direct the mobilized electrons towards the anode front contact, which is usually transparent conductive oxide (TCO) [22], [28]. Material-wise, the most commonly used materials for the transport layers are Spiro-OmeTAD (Spiro), NiO, and CuO for the HTL and TiO_2, SnO_2, and SiO_2 for the ETL [28]. Coatings may be added to reduce reflection, increase the photon path length and prevent potential degradation [65].

The simulated solar cells are, as depicted in Figure 2.3, $MAPbI_3$ perovskite TFSCs cells built upon a silver substrate, by default possessing a Spiro HTL and a TiO_2 ETL, encapsulated by an ITO ARC [66]. Three different ARC geometries were subjected to optimization: a planar layer, an array of nanopillars and a grid of crossed gratings. Their optimization is defined by the fine-tuning of the geometrical properties that define these layers. For the planar PSCs, optimization depends solely on the thicknesses of its transport layers and ARC. For the three-dimensional coatings, three extra variables are considered, namely the pitch, width, and height. The stipulated pitch, the measurement by which the repeating unit cells are separated, is defined as a multiple of their width; for instance, a pitch of 1 implies the units have no separation in between them, and a pitch of 2 would result in a gap matching the width.

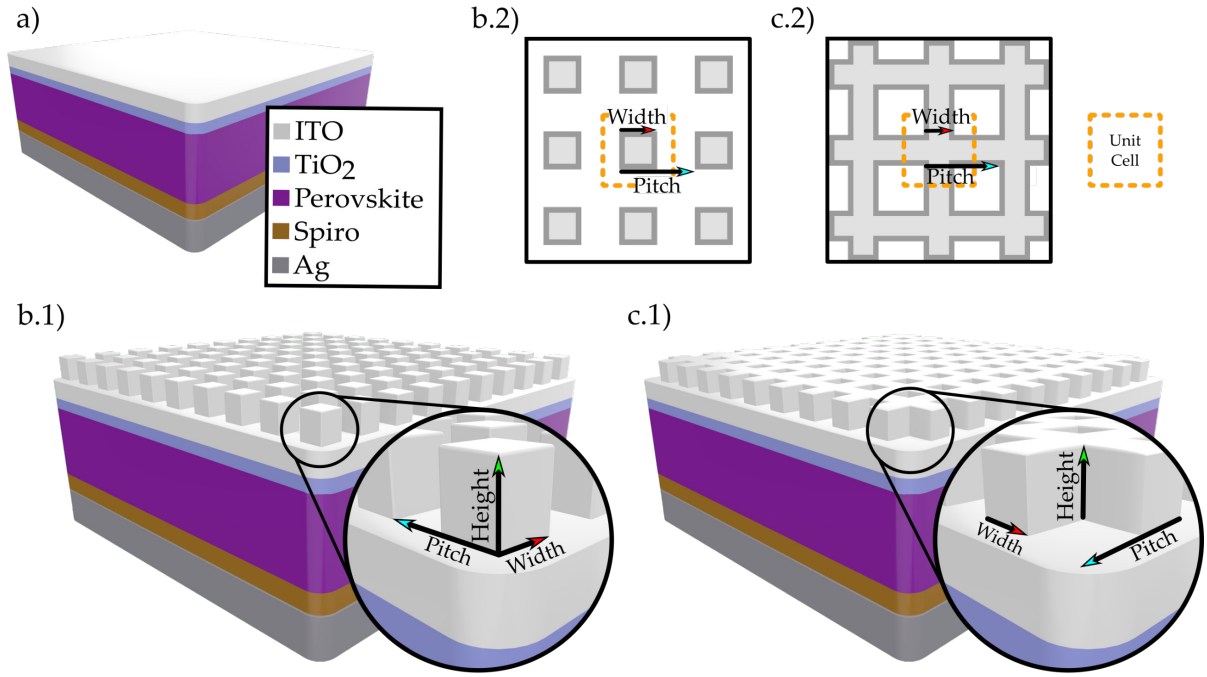

Figure 2.3 – 3D Rendering of the simulated MAPbI3 perovskite solar cells with planar (a), nanopillar (b.1) and crossed grating structures (c.1) with illustrative zoom-in renderings of the photonic structures subject to optimization and top-down schematics of the simulated nanopillar (b.2) and crossed gratings unit cells.

Since polarization and viewing angles are not taken into consideration when accruing the reflection spectra, symmetry must be preserved in the plane perpendicular to the incident radiation. Therefore, the nanopillar grating pitch is kept consistent on both normal axes. Both the fixed parameter values and the optimization ranges are presented in Table 2.1.

Table 2.1 – Table containing the structural parameters of the structures in question. The values within square brackets are the upper and lower bounds of the optimization ranges. Pitch is given as a multiple of the width.

	Ag	Spiro	Perovskite	TiO_2	ITO	Width	Height	Pitch
Planar	150 nm	[50-200] nm	500 nm	25 nm	[50-200] nm	-	-	-
Nano Pillars						[50-200] nm	[0-500] nm	[1-3]
Crossed Gratings								

The values pertaining to the simulated refractive indexes of the ITO, TiO_2, perovskite, Spiro, and Ag layers were sourced from Konig et. al [67], Siefke et. al [68], van Eerden et. al [69], Filipič et. al [70] and E. Palik [71], respectively, presented in Appendix A. Both the real and the imaginary refractive index curves are plotted in Figure A.1 while the curve fitting parameters used to interpolate the aforementioned experimental data are listed in Table A.1.

3

RESULTS AND DISCUSSION

3.1 Initial Developments and Method Validation

Given the novelty of the concepts and structures herein described, a series of precursory experiments were conducted to ensure that these results could be deemed viable and reproducible. Firstly, the colour distance metric was tested, secondly, the applicability of the CIE method was evaluated, and finally, a baseline set of simulation results was compared to the analytically solved counterpart.

3.1.1 Colour Distance Tests

To appraise the validity of the Euclidean distance method as a means of quantifying the differences between two colours, a list of 128^3 RGB codes were generated to define a colour space between absolute white (with coordinates 0, 0, 0) and absolute black (255, 255, 255). Each of these codes is evenly distanced by a factor of two degrees of separation from any other given point in this three-dimensional space. By this metric, the highest possible separation between any two colours would be approximately 441, as given by the distance between absolute white and absolute black. As previously mentioned, the perception of colour and subsequently the difference between colours is highly subjective, nevertheless, the existence of an objective metric, albeit unitless, is necessary to home the optimizing particle swarm on the chromaticity closest to the desired colour. The distances between each point in this generated array and a set of chosen colours were then calculated. This set comprises the extremes of each axis of the RGB space, absolute black, absolute white, and an arbitrarily chosen intermediate point with RGB values (255, 105, 180), henceforth referred to as pink. Figure 3.1 shows the effectiveness of this method in distinguishing different colours. When taking into consideration the three primary colours, an average observer would have difficulty distinguishing between any two

colours within 30 points of the original value. A side effect of interpreting RGB codes as a set of Euclidean coordinates is the fact that every distance value is representative of a spherical surface centring on said RGB value and possessing a radius equal to the distance value. This means that for any given colour, provided that the distance value is large enough, two noticeably different hues may be assigned the same distance value. This explains the pronounced variations in chromaticity and lightness for the most distant points in the subplot in Figure 3.1 – e.g., the shifts from green to yellow in the blue chart. This variance is mostly trivial for PSO, as these shifts in hue become progressively less pronounced as the swarm closes in on a particular point.

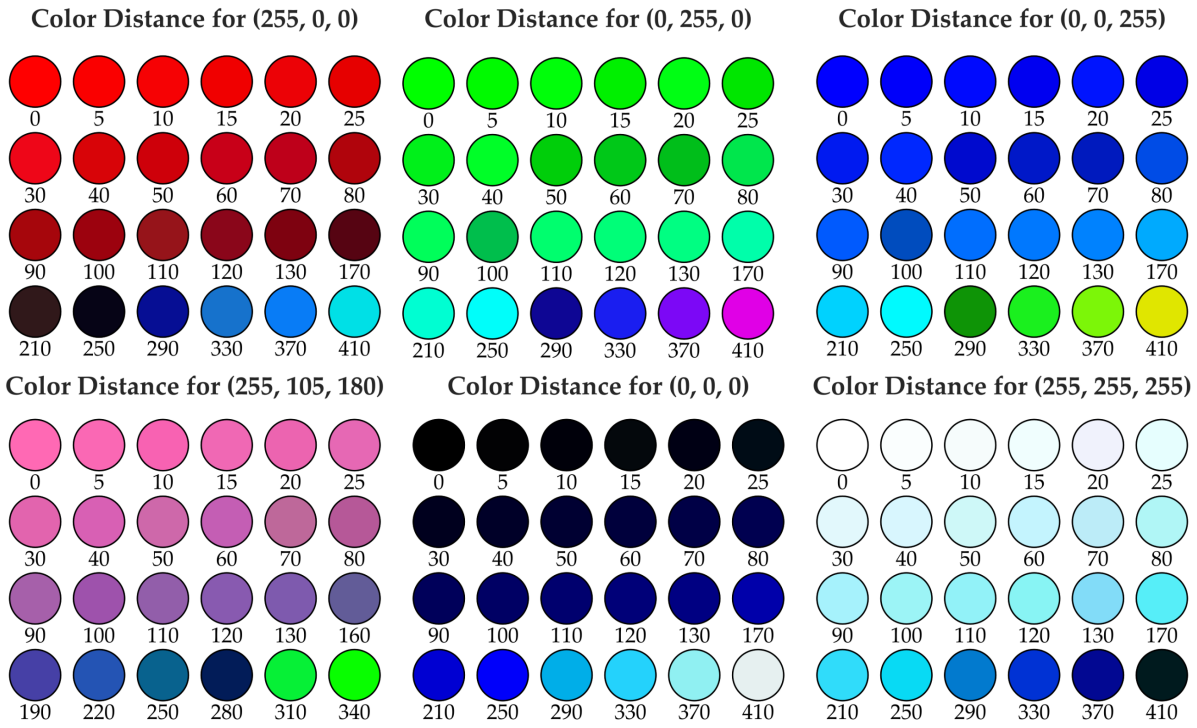

Figure 3.1 – Colour Distance Charts for mono-red, mono-green, mono-blue, absolute white, absolute black, and pink Each chart consists of 24 coloured dots with colour distances increasing left to right, top to bottom from the original colour. Each coloured dot is labelled with its corresponding colour distance value.

From Figure 3.1 it is possible to verify that the determining factor when calculating the distance to absolute white (or absolute black) is lightness, not hue. For instance, the white and black charts show a progression in different shades of blue, but any coloured dot could be replaced by another, equally light and therefore equally distant, shade of either red or green. Since the chosen method for reflection spectrum to colour conversion neglects the information pertaining lightness of the reflected colour, there is no chance that the optimizing algorithm might erroneously converge on an equally light colour to the detriment of its chromaticity.

3.1.2 CIE Method Validation

Spectra pertaining to another parallel experiment conducted by PhD Student Jenny Boane were tested to demonstrate the viability of the CIE method as a tool to convert reflectance spectra into RGB colour values. Said experiment sought to study the effects of varying TiO_2 thickness values on the colour of a PSC and its encapsulant layer and provided data for the reflectance spectra of each specimen as well as photographs of the specimen itself. After levelling the data to match the tristimulus array, the extrapolated colour for each specimen is shown in direct comparison with the provided pictures in Figure 3.2.

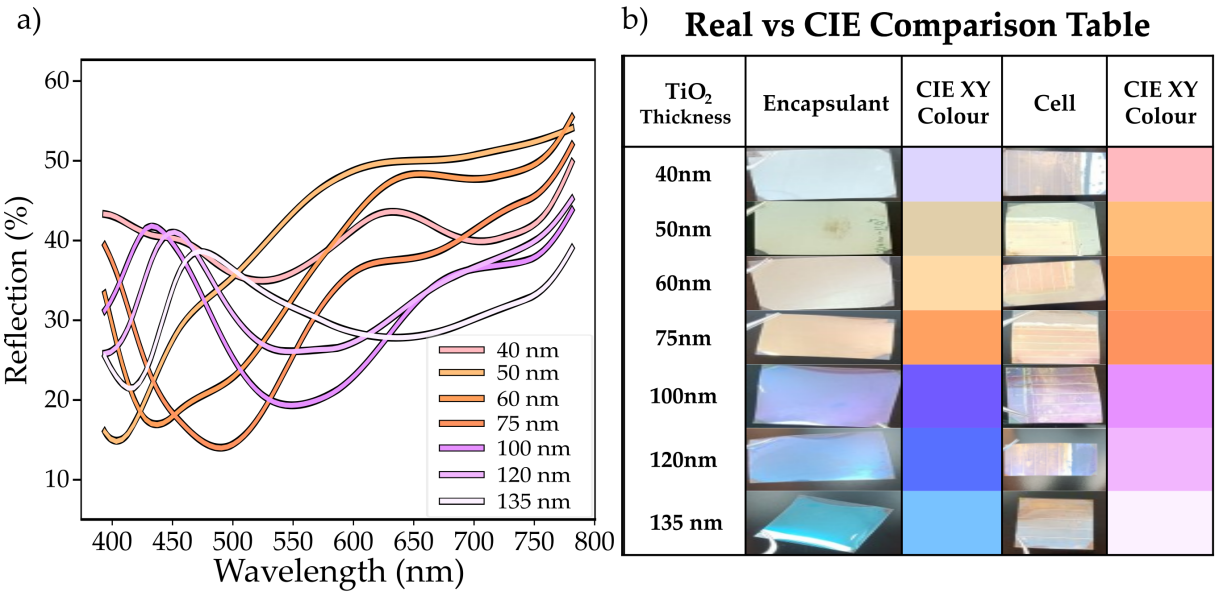

Figure 3.2 – Measured reflection profiles for bare PSCs with varying TiO2 thickness (40, 50, 60, 75, 100, 120 and 135 nm). The colour of each line represents the CIE determined colour. b) Table comparing the CIE colour to the actual colour of the devices for bare (reflection profiles shown in a)) and encapsulated PSCs with varying TiO2 thickness. Each photo of the device is accompanied at its right by the respectively calculated CIE colour.

In Figure 3.2 b) one can see that the simulated colour closely follows the actual colour of the device. There is, however, one notable exception in the 135 nm Cell specimen, whose anomalous response is plausibly a side effect lack of sensitivity of the CIE XY method to the lightness factor. This effect, as per Chapter 2.2 , often translates into seemingly muddled, pale colours, whenever the analysed spectrum lacks any distinguished peaks in the visible light interval. This explanation, accompanied by the reflectance curves illustrated in Figure 3.2, is congruent with the fact that the colour derived from the spectrum corresponding to the isolated 135 nm encapsulant is much clearer and consistent with the preceding thickness values. Nevertheless, these imperfections are negligible as the PSO algorithm is designed to circumvent them altogether, as previously noted.

3.1.3 Preliminary Simulations

The base FDTD model (purely planar simulation) needs to be first compared with the analytical results to guarantee the validity of the results. This validity depends on the stability of the script of the coded model as well as the adequacy of the optical data fits of the simulated materials, which are adjusted by varying the Fit Tolerance and the Max Coefficients within the Lumerical Material Database, listed in Table A.1 of Appendix A. Figure 3.3 displays a graphical comparison between the simulated and analytically derived curves for a sample planar structure with layer thicknesses of 250 nm for both the Spiro and the ITO layer. From here it is determined that the simulated results closely match their analytical tie-ins for most of the analysed spectrum, apart from a minor discrepancy localized in the 760 to 800 nm range; this deviation peaks at a modulus of 6.45% at 780 nm, a value which falls within the acceptable error margins. Additionally, parsing these curves through the CIE colour conversion function enables the comparison to the extrapolated colours in the figure. Notably, there is a virtually indistinguishable difference between the CIE Colours extrapolated from either method.

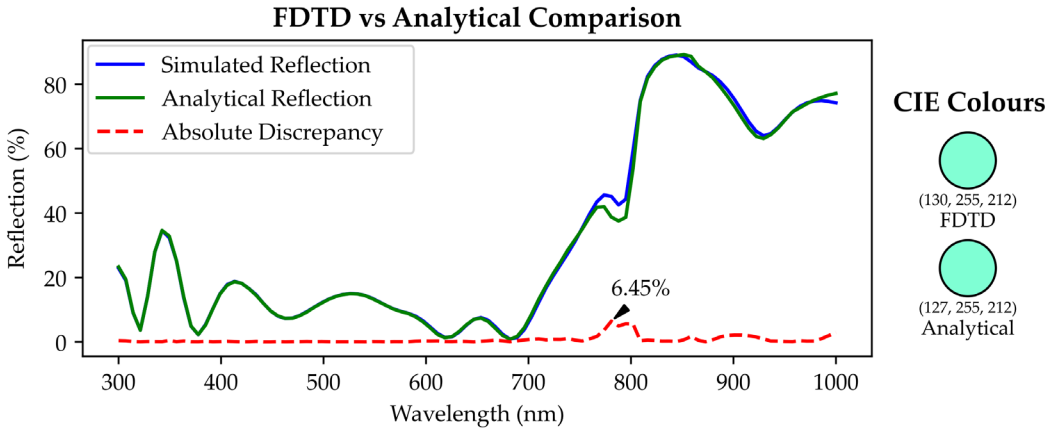

Figure 3.3 – Reflection profile used to validate the numerical FDTD-obtained results for the base cell. In blue it is shown the FDTD calculation and in green the analytical result. The red dashed line represents the relative absolute between both results. The rightmost elements represent the CIE determined colour for both the FDTD (top) and analytical (bottom) results.

The selection of FDTD Lumerical simulation settings, most notably mesh accuracy, mesh refinement, and the number of frequency points, is contingent on a consensus between settings employed in previous publications and the results of a series of convergency tests; a comprehensive list of the most relevant simulation settings is detailed in Table B.1 of Appendix B.

3.2 Planar Sweeps

The purpose of these sweeps is threefold. Firstly, it serves to highlight the existence of any anomalies in the construction of the solar cell model or in the functions of the said model. Secondly, sweeping the planar structure in terms of Spiro and ITO layer thicknesses provides a comprehensive set of results that can be visualized in the form of heatmaps in Figure 3.4, and that can be used as a base to evaluate the upcoming PSO results. Lastly, it serves to set expectations for what is possible within the given simulation ranges and conditions through a comprehensive rendering of each combination of simulation parameters within said linear space. For instance, the colour map depicted in Figure 3.4 a) shows the parameter ranges where certain colours are generated, and ultimately encompasses the full spectrum of possible RGB values. This sweep encompassed the full range of both relevant optimization parameters — Spiro and ITO layer thicknesses — within a linear space divided into 30 intervals.

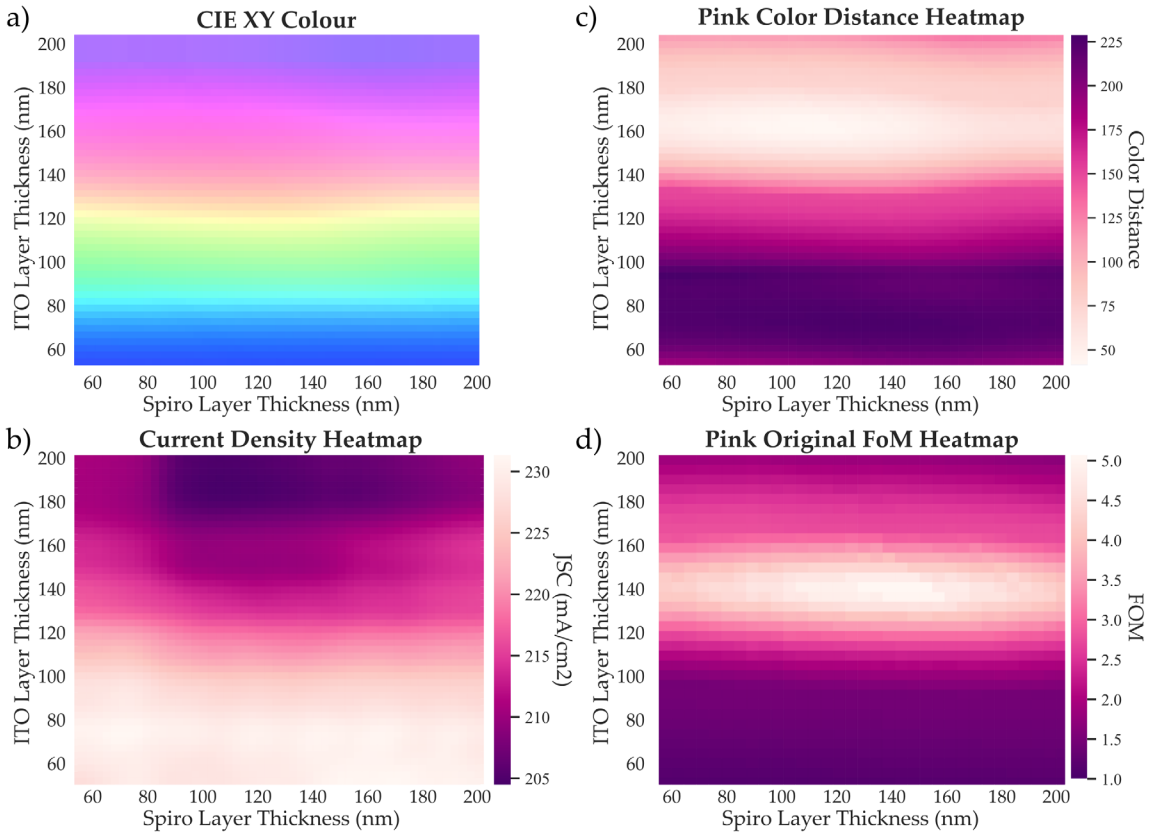

Figure 3.4 – Heatmaps for the simulated CIE XY colour (a) and J_{SC} (b) of the planar structures within the allotted parameter ranges and the resulting colour distance (c) and FoM (d) heatmaps obtained when aiming for pink. This data is obtained via parameter sweep through the ranges in Table 2.1 in 30 evenly spaced steps for either parameter.

The colour map in Figure 3.4 a) also shows that the ITO thickness has a greater impact than the Spiro thickness in the reflected colour, as seen in the horizontal colour homogeneity

for fixed ITO thickness values. This is to be expected since the Spiro layer interacts solely with wavelengths which are not reflected or absorbed by the upper layers. There is an argument to be made here in favour of setting the Spiro thickness value to an already proven optimal value, in accordance with previous publications [66]. The elimination of this optimization parameter could potentially reduce the simulation run time, but ultimately more data is needed to ensure the redundancy of this parameter in the case of the more complex structures. This speculated redundancy is further explored in Chapter 3.5. When optimizing for pink, the FoM heatmaps in Figure 3.4 show that a properly functioning PSO algorithm should converge in the 157-172 nm range and 65-142 nm range for the ITO layer thickness and the Spiro layer thickness values respectively; the comparatively wide breadth of the latter range highlights the weak link between Spiro layer thickness and CIE Colour.

3.3 Particle Swarm Algorithm Design

Besides the velocity adjustment factors previously discussed in Chapter 2.4, the PSO is defined by the minimum and maximum number of iterations, the number of particles, and optionally by a set of search stagnation criteria. These factors vary slightly depending on the complexity of the problem, ergo a preliminary comparison of different factor combinations is usually required even if some of these values can be roughly generalized based on existing literature [59], [72]. Notably, it is important to guarantee that the number of iterations is high enough for convergence to occur, but not so high that the particles stagnate before effectively exploiting the area around the best determined value between all the particles in the algorithm (*gbest)*. Additionally, since the total number of simulations is given by the number of particles times the number of iterations, needlessly increasing either of these factors will potentially result in a substantial loss in computing time and resources [72]. Precautionarily, a search stagnation criterion is pre-established to automatically conclude the optimization under the conditions that a minimum number of iterations have been completed and no improvement has come about within a set number of iterations.

Table 3.1 – Table of PSO optimization factors. The values within brackets are the upper and lower bounds considered for the parameter optimization range.

	Social Learning	Cognitive Learning	Inertia Weight	Iterations	Tolerance	Number of Particles
Value	**1.49**	**1.49**	**[0.9-0.4]**	**[50-100]**	**10**	**25**

The factors chosen for preliminary testing are based on existing literature [59] and are displayed in Table 3.1. PSO algorithms differ based on how information is disseminated across the swarm. The *gbest* topology herein is characterized by allowing all the particles to know the current best parameters. Contrarily, other PSO variants restrain the flow of information within a certain proximity, pre-established or adaptive hierarchy, or through random connections [73]. A downside to the straightforwardness of the *gbest* method is its ensuing susceptibility to premature convergence unto a suboptimal relative maximum [61]. This effect can be lessened, if not entirely prevented, through case-specific tuning of inertia and social learning factors [72], [73]. The PSO Python script underwent a series of iterations, and the finalized version is contained in Appendix C.

3.4 Figure of Merit Selection

To select which FoM would be best suited to optimizing for both colour and current density, multiple PSOs were executed for each combination of photonic structure geometry — planar, nanopillar and crossed gratings — and desired colour — pink, green and red. As previously discussed on page 17 of this work, pink is a colour which is exhibited by a wide array of Spiro and ITO layer thickness combinations, at least in the case of the planar PSCs. Batches of several optimizations (5 for pink and 3 for red and green) were used to test the algorithm's aptitude for convergence. This exposes the algorithm to the broadest amount of possible optimal results. Furthermore, since the PSO is initially a stochastic method, the effects of the randomization of starting parameters and respective velocities were assessed by fixing five sets of starting conditions that were then used in pink-seeking nanopillar-based optimizations of either FoM.

3.4.1 Planar Comparisons

Planar optimizations were done primarily to prove that the PSO algorithm was prioritizing the same area as the results presented in Chapter 3.2. For the sake of preserving optimization factor uniformity across all experiments, the planar PSOs initially used the same 25 particles for 50 iteration optimization scale intended for the other (more complex) problems; this meant that the planar optimizations required more data points than the original planar sweeps — which simulated 900 evenly spaced points as opposed to the 1250 simulations performed by this PSO — while providing no new information. The PSO algorithm is designed to optimize

for multiple variables at once, meaning that this inefficiency is not relevant in the upcoming, more complex, scenarios. The sheer volume of particles simulated incidentally masked a minor error in the velocity update section of the PSO code, though this flaw would be later identified and fixed when analysing the nanopillar PSO results. Nevertheless, it was proven that the algorithm could accurately identify which points to prioritize.

3.4.2 Nanopillar Comparisons

The bulk of the PSO algorithm development and testing was made on the nanopillar structures, as these were estimated to be sufficiently complex to highlight any underlying flaws in the optimization script while also keeping runtimes relatively brief. Since the PSO method possesses a degree of inherent randomness, the comparison of the two FoMs was firstly calculated using a set of 5 fixed seeds applied to the random number generator pre-packaged with Python. In this manner, both the "Original" and "Root" FoM-based PSOs start with the exact same set of particles and velocities.

Figure 3.5 proves that each method has the potential to reach its own conclusion, which in some cases wildly disagrees with the opposing method, even if both had the same starting points. This means that ultimately, it is the FoM and its subsequent convergency pattern which dictates the result, not the randomized starting conditions. Furthermore, the table presented

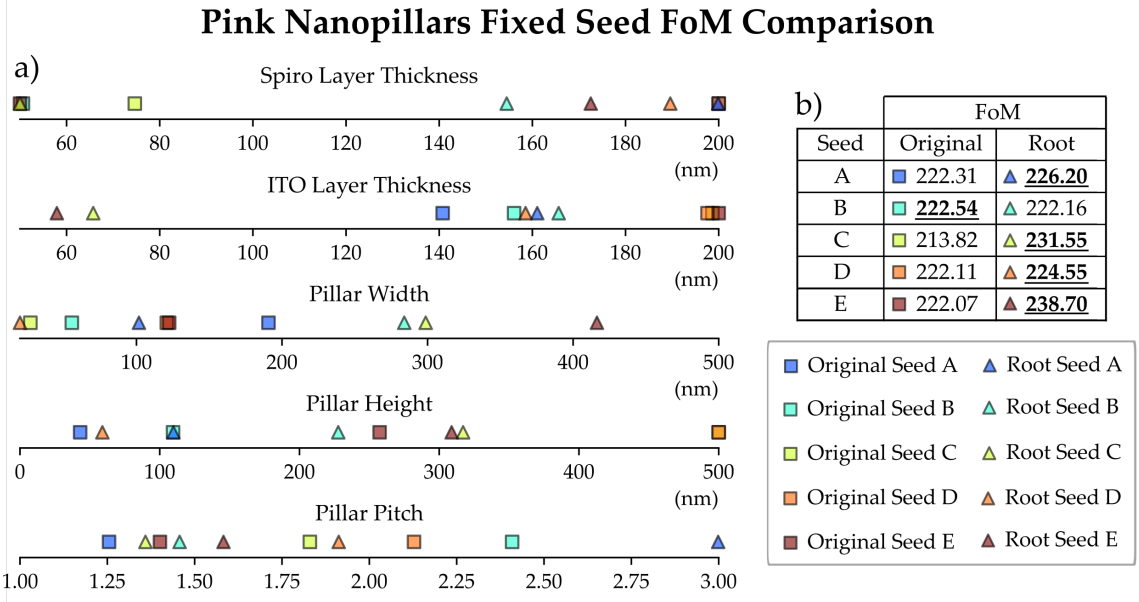

Seed	FoM Original	FoM Root
A	222.31	**226.20**
B	**222.54**	222.16
C	213.82	**231.55**
D	222.11	**224.55**
E	222.07	**238.70**

Figure 3.5 – Comparison in FoM performance between two sets of fixed seed pink seeking nanopillar optimizations. Each seed is represented by a letter and a colour to compare between the results obtained via the Original (depicted by squares) or Root FoM method (triangles). The comparisons are established by 5 sets of one-dimensional plots containing the best values obtained for each parameter (a) and their respective normalized FoM values are displayed in table (b), with the best of each seed being underlined and emboldened.

in Figure 3.5 b) highlights the differences between the final FoM value for each method. In most cases, the Root FoM overperformed relatively to the Original FoM. In terms of defining an optimal configuration for pink nanopillar structures, these results are somewhat inconclusive, as the PSO seems to be converging on multiple combinations of parameters corresponding to local maxima. Nevertheless, the PSOs managed to emulate the intended colour within a virtually indistinguishable margin of ≤ 1 colour distance unit, albeit with varying Jscs.

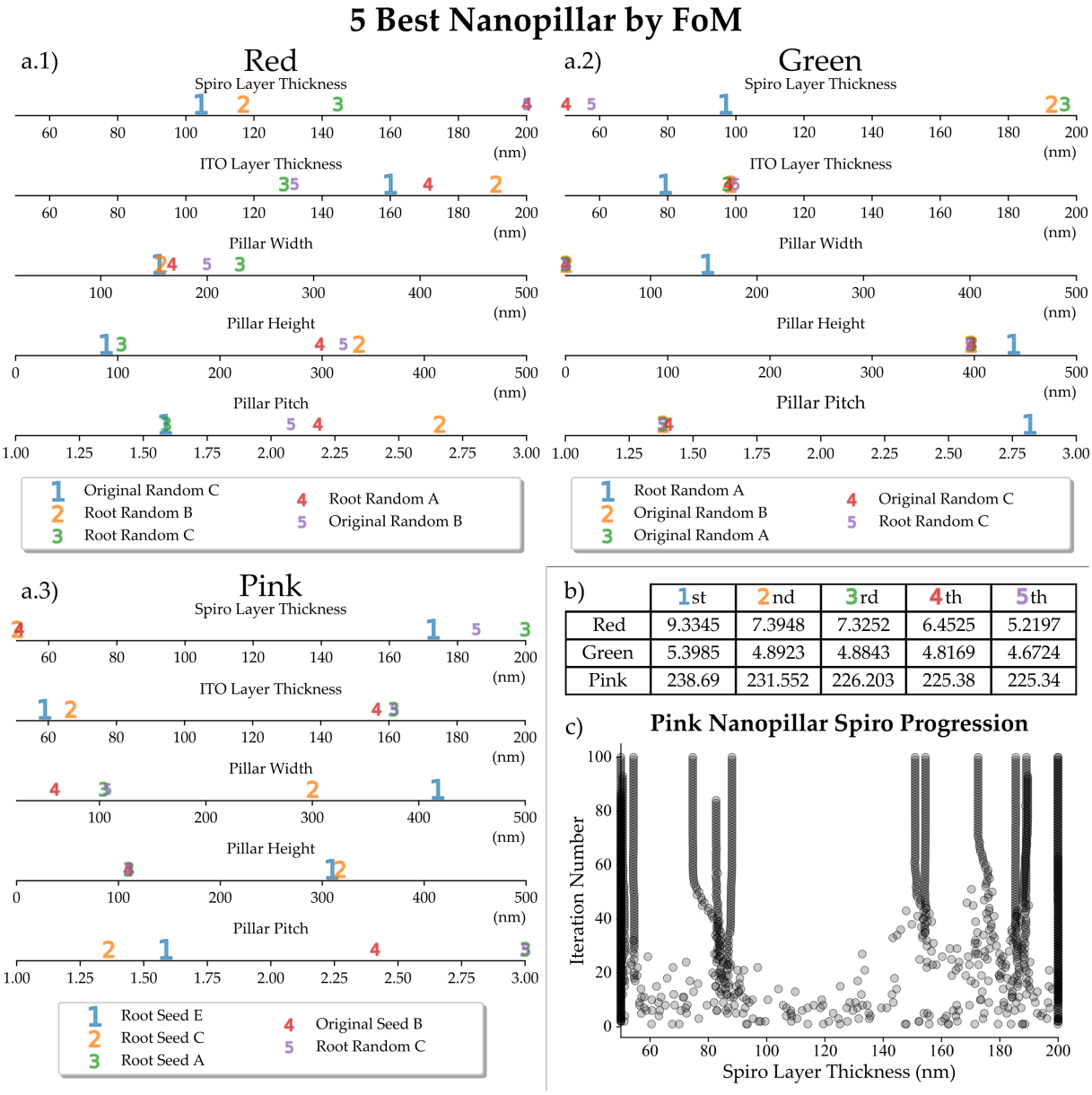

b)	1st	2nd	3rd	4th	5th
Red	9.3345	7.3948	7.3252	6.4525	5.2197
Green	5.3985	4.8923	4.8843	4.8169	4.6724
Pink	238.69	231.552	226.203	225.38	225.34

Figure 3.6 – Summary of the 5 best nanopillar PSOs results (considering both Root and Original FoM) for (a.1) red (a.2) green and (a.3) pink. The number and size represent the ranking for each FoM among all the results. b) Normalized FoM for each of the 5 best PSOs and for each colour. c) Particle position for the Spiro layer for each iteration of both pink nanopillar optimizations.

Figure 3.6 plots a.1 through a.3 comprise most of the relevant data extracted from the FoM Comparison trials in nanopillars seeking red, green, and pink, respectively. In the case of the red nanopillars, a clear preference for a specific range of pillar widths is shown; the ITO layer thickness is relegated to the thicker half of the range, indicating that while there is a bias for these values, the peaks in this region may not be as prominent; contrastingly, the pillar height and the pillar pitch parameters both tend to accumulate around two local maxima. The best results are found in the 90 to 110 nm range for the pillar height and 1.5 to 1.65 range for the pillar pitch, while the 2nd best results are present in the 300 to 400 nm range for the pillar height and the 2 to 2.75 range for the pillar pitch. Similar inferences may be established when looking at the 5 best results for the green nanopillars, except in this case the close-range biases are found in the ITO layer Thickness and pillar height parameters, while the pillar width and pillar pitch parameters are seemingly divided into two local maxima. As previously stated, the colour pink is seemingly produced by multiple different configurations of nanopillars (within these parameter ranges), and thus these results might have been deemed inconclusive were it not for the sheer difference in FoM value between the 1st, 2nd and 3rd best configurations, detailed in Figure 3.6 table b). In this analysis, the Spiro layer seems to have a weak correlation to the FoM as its value tends to fluctuate throughout the entire range. An argument could be made that, at least in the case of the pink nanopillars, there might be two local maxima situated at the edges of the parameter range.

Figure 3.6 Graph c), which depicts the progression of the best parameters at any given iteration number for all the pink nanopillar runs combined, shows that, at least in the earliest stages of the optimization process, most points in this range are deemed to be "optimal", furthermore strengthening the argument in favour of ruling out the relevancy of this parameter. The optimization setting used for Figure 3.6 will generally go beyond 80 iterations. However, the particle position development makes it clear that passed 60 iterations, the FoM improvements are mostly marginal (less than 1%). Hence, the algorithm was updated to include a tolerance value. Unless the change in FoM between iterations passed the tolerance value (default of 5%), the optimization algorithm would stop earlier to greatly reduce optimization time at a minimal performance cost. This is further detailed in Figure 3.7 a) which shows the increases in FoM in function of the iteration number for the best case for the pink nanopillars. The minimum iteration value is kept unchanged, as the data gathered from the previous PSOs indicates that the most relevant improvements can happen as late as the fiftieth iteration. A notable case during this study was seen in the velocity update part of the particle

swarm where a minor design flaw in the section of the PSO code responsible for updating the velocity matrix at the extremities of the range, which lead to the accumulation of particles at the borders of each range as seen in Figure 3.6 Graph c). While the particles in the PSOs affected by this issue were not allowed to escape their range, their associated velocities would be preserved even as they hit these walls, meaning that their inertia would ultimately trap them alongside the border conditions.

Figure 3.7 b) illustrates this through contrast with the velocity for a set of particles converging away from the range extremities. In Figure 3.7 b), the leftmost graph demonstrates the ideal oscillating pattern— where particles are pulled back and forth in alternating positive and negative velocities around the best value, unlike what happens in the rightmost graph. The random nature of the PSO algorithm can obfuscate some errors in the code base. This portion of the code was updated, and the results presented henceforth, save for the upcoming pink gratings FoM comparison, were obtained from a fixed version of the PSO algorithm.

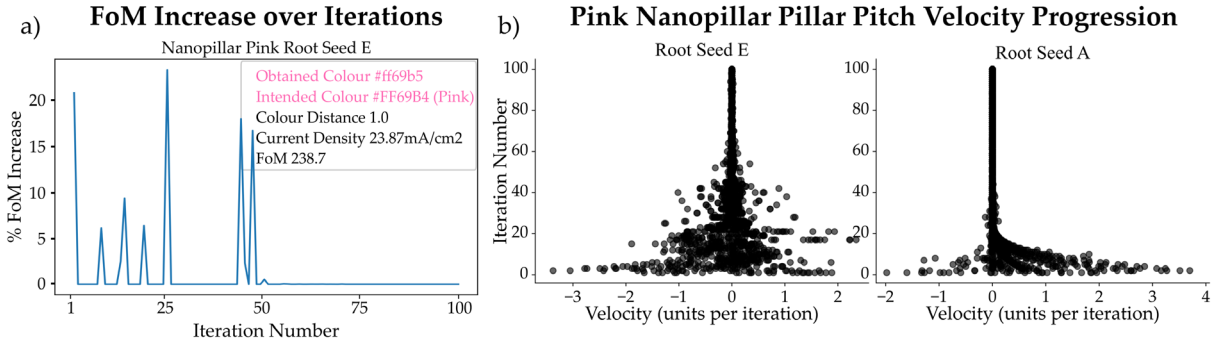

Figure 3.7 – a) Percentual FoM Increment relative to the finalized maximum FoM fitness for the Nanopillar Pink Root Seed E PSO, the best out of the initial 20 PSOs done for pink nanopillars; b) Progression in the Velocity of the Swarm Particles alongside the "pillar pitch" axis for the pink Nanopillar Root Seed E and Root Seed A.

3.4.3 Crossed Grating Comparisons

Besides the information regarding the supposed optimal parameters for each development, the plots in Figure 3.6 are also indicative of the comparative suitability of each FoM method. To ensure that the FoM selected method suits the crossed gratings scenarios, 8 more PSOs were executed, 4 for each method optimizing for pink as presented in Figure 3.8. When looking at the five best results, the conclusions drawn here are similar to those of the pink nanopillars: most parameters either converge within a specific range, as is the case with the ITO layer thickness and the pillar pitch or are divided between two or three peaks. Additionally, these results once more proved that the Root method outclasses the Original counterpart. This is thought to be a consequence of how the Root method places less emphasis on minimizing the

colour distance, meaning that the Particles are more likely to make decisions based on maximizing the J_{SC}, thus preventing premature convergence on subpar FoM peaks. It also is worth noting that the crossed gratings marginally underperformed in this stage marginally underperformed in this stage in comparison with the nanopillar structures.

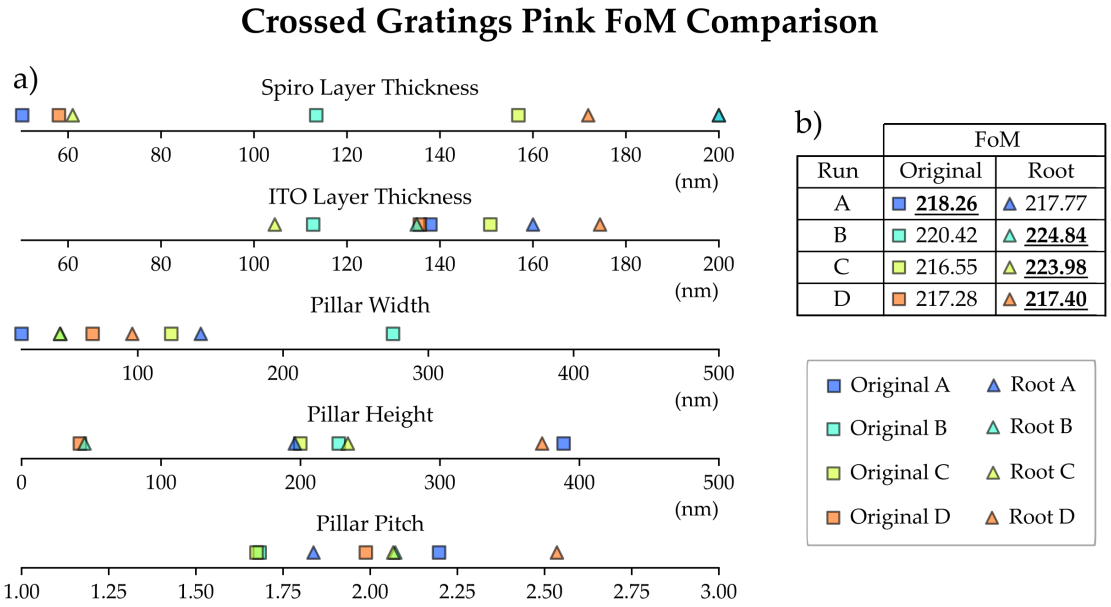

Run	FoM	
	Original	Root
A	**218.26**	217.77
B	220.42	**224.84**
C	216.55	**223.98**
D	217.28	**217.40**

Figure 3.8 – Crossed Gratings FoM comparison for four trials of each FoM method on randomized seeds. Original FoM optimizations are represented by squares while Root FoM optimizations are represented by triangles. Normalized FoM values are listed in table b).

3.5 Parameter Filtering Sweeps

Two parameter sweeps, depicted in Figure 3.9 and Figure 3.10 were performed to ascertain whether the Spiro layer Thickness should be excluded from the next set of PSOs. Each of these

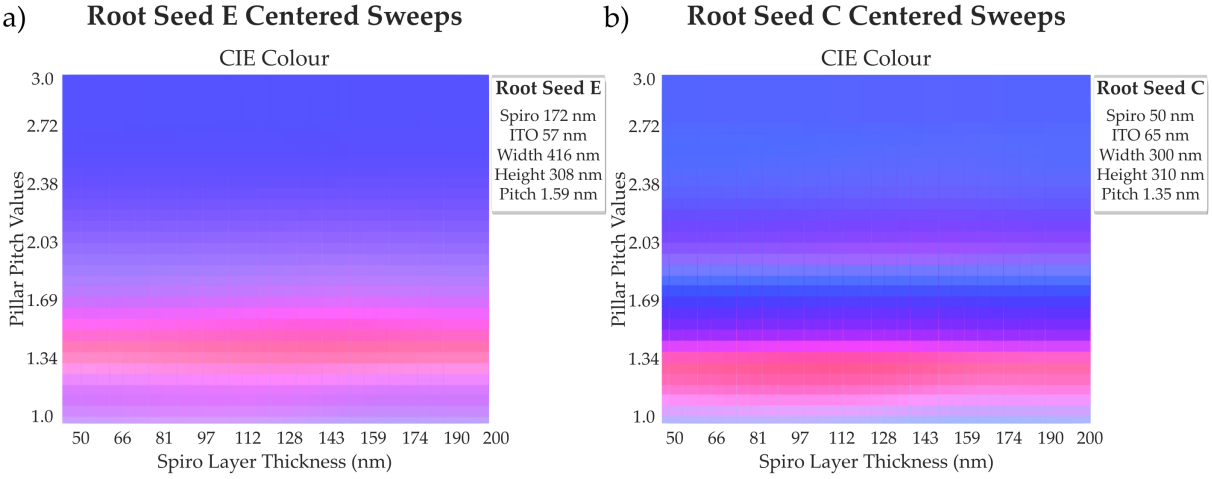

Figure 3.9 – CIE Colour maps for pink nanopillar structures centering on the geometries of the Root Seed E results (a) or the Root Seed C results (b), varying Spiro Layer thickness and Pillar Pitch Values.

sweeps varies the Spiro layer Thickness value in conjunction with the pillar pitch values, with each of the other parameters set to match the best and the second-best set of parameters for pink nanopillars. The first pair of heatmaps in Figure 3.9 shows the chromaticity spectrum contained within these optimization ranges, while the first pair in Figure 3.10 shows the current density generated by each combination of pillar pitch and Spiro values under each set of fixed ITO, pillar width and pillar heights. Finally, the second pair of heatmaps in Figure 3.10 shows the variation in Root FoM for either scenario within the pitch-Spiro sweep.

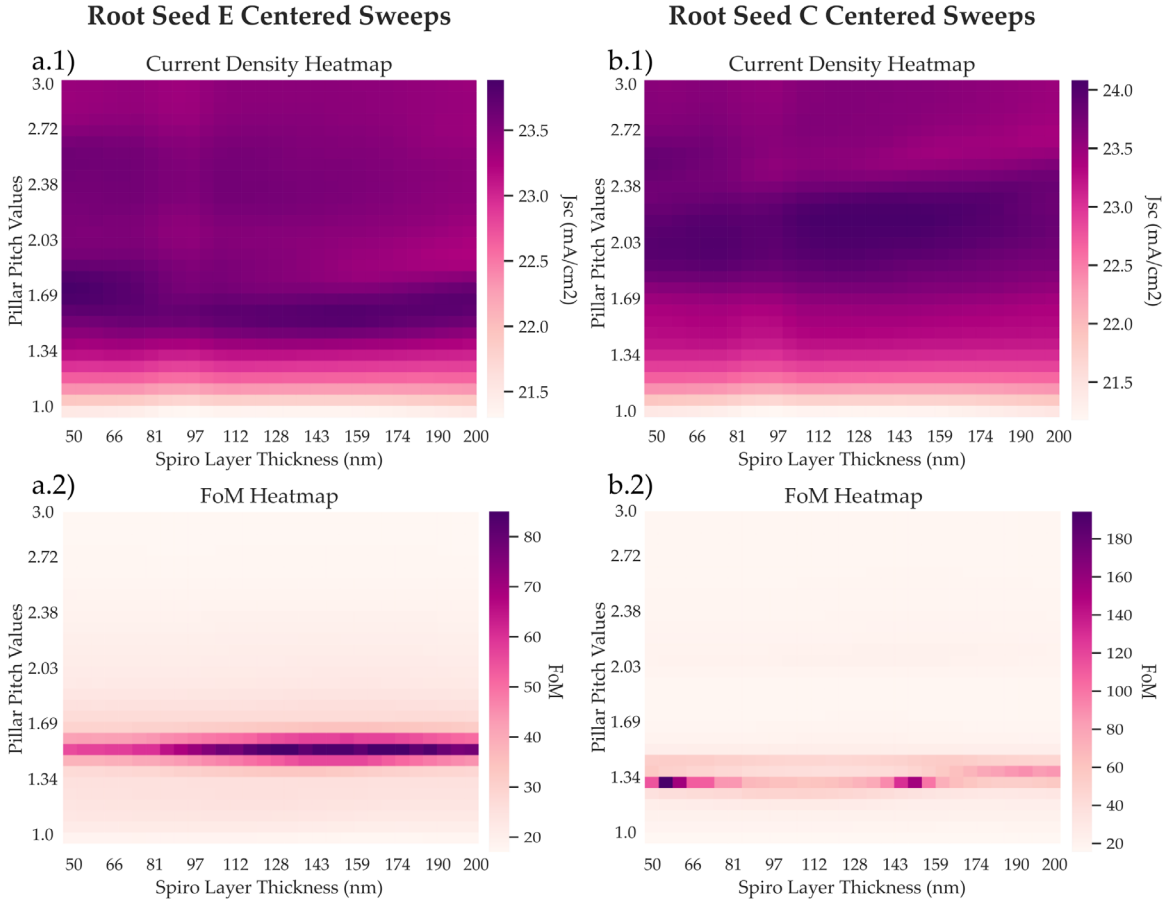

Figure 3.10 – Current Density Heatmaps (a.1, b.1) and FoM Heatmaps for pink nanopillar (a.2, b.2) structures based on the geometries of either the Root Seed E results (a) or the Root Seed C (b) results, varying Spiro Layer thickness and Pillar Pitch Values. Heatmap colour gradient darkens with the increase in performance.

In either case, the optimal FoM can be approximated to a thin line running parallel to the Spiro axis, meaning that the performance of the cell is mostly dependent on pillar pitch values. This is attributed to the fact that the Spiro layer exhibits minimal interaction with the incident light, due to it being placed underneath the perovskite absorber layer. Therefore, given the weak link between Spiro layer Thickness and the best FoM values, for the sake of simplicity, all further simulation results henceforth presented are based on a fixed value of 150 nm for the Spiro layer thickness.

3.6 Zoom Particle Swarm Optimizations

The next step in obtaining the optimal set of parameters is to restrict the optimization ranges to exclude the suboptimal local maxima, thus making it so that the "zoomed-in" particles are more likely to home in on the true optimal values. This is an intermediate process, and the number of PSOs per batch is subject to the data analyst's judgement. Ideally, this step should be repeated until some level of certainty can be had regarding either the next best set of ranges or until a second split in local optima is found. The first set of zoomed-in parameter ranges was based on the five best results obtained in the FoM comparison stage for each combination of structures and colours, favouring the data gathered from the Root PSOs and fixing spiro layer Thickness values to 150 nm as previously mentioned. Figure 3.11 depicts a successfully zoomed-in PSO based on the 5 best results for the pink nanopillars. The data gathered from this intermediate stage should suffice to determine a new set of even more restrictive parameter ranges that define the final PSO. Notable restriction measures include:

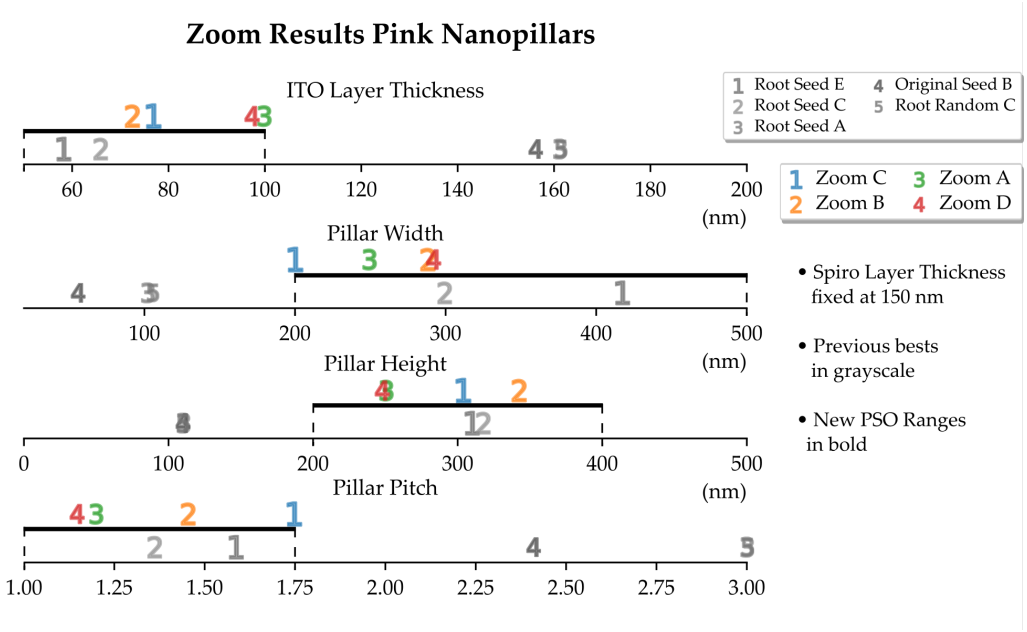

Figure 3.11 – Next generation of optimal PSO Parameters for pink nanopillars resulting from a set of restrictions on the width of each parameter range depicted in bold. The previous top 5 are left in grayscale for comparison.

- In the case of the pink nanopillars, rather than exclude the 3rd and 4th best results from the final PSO, these parameters were kept, partly due to their proximity to the 1st and 2nd best results, but also because the 4th coincided with the 2nd in pillar width.
- Regarding the pink nanopillars, the final pillar pitch ranges were designed to extend slightly past the uppermost border of the intermediate zoom step to allow the swarm to further explore the area surrounding the 1st best result. This exception was deemed unnecessary in the case of the pink nanopillars pillar width, as there was less ambiguity

stemming from the dispersion in the best results in this stage.

- In some scenarios, as was the case with the pink gratings pillar width ranges, the first stage of zooming was prematurely defined too narrowly to allow for further amplification — based on the physical principles of light interference, structural changes of magnitudes on the scale of single nanometres should not cause relevant variations in FoM; thusly, this range was kept between the intermediate and the final zoom steps.

3.7 Final Optimized Parameters

Table 3.2 showcases the efficacy of this method of obtaining the ideal parameters for the obtention of colour in the solar cells for the structures depicted in Figure 2.3.

Table 3.2 – Table containing the final optimized set of parameters for each combination of structures and colours. The generated CIE colours are illustrated next to their respective hexcode identification. Pillar Pitch is given in multiples of the Pillar Width.

Final Results

Structures	Desired Colors	Spiro (nm)	ITO (nm)	Pillar Width (nm)	Pillar Height (nm)	Pillar Pitch	CIE Colour	Colour Distance	JSC (mA/cm2)
Baseline		150	250				#68fff6		21.350
Planar	**Pink**	103	158				#ff88d8	47.508	21.216
	Red	106	153				#ff95cf	255.049	21.332
	Green	50	105				#8cffa9	219.450	22.852
Nanopillars	**Pink**	150	85	282	282	1.49	#ff69a4	1	23.355
	Red		139	237	104	1.63	#ff181a	35.386	23.341
	Green		79	159	431	2.63	#16ff1a	34.059	23.654
Crossed Gratings	**Pink**		137	89	43	2.39	#ff68b4	1	22.363
	Green		108	137	354	3.00	#27ff44	78.390	22.299

Compared to a baseline structure utilizing standard layer thicknesses, the optimized solar cells were capable of exhibiting simulated colour and, in most cases, there was also a considerable increase in current density, produced by the same LT structures that selectively reflect part of the solar spectra. Remarkably, the more complex nanopillar and crossed grating structures were capable of exhibiting colours that were otherwise impossible within these given parameter ranges for the planar configuration, as per Figure 3.4. Comparing the reflection curves of the baseline structure with the reflection curves of the optimal green and red nanopillars serves as further proof that the structures herein described are effectively reflecting selective portions of the solar spectrum to produce structural colour. In Figure 3.12, the reflection curve for the baseline structure possesses amorphous peaks scattered through the spectrum, while the other curves are more focused, with the optimal green nanopillar

curve evidently reflecting wavelengths of higher energy than its red counterpart, though both curves increase significantly as the photon energy approaches the perovskite bandgap.

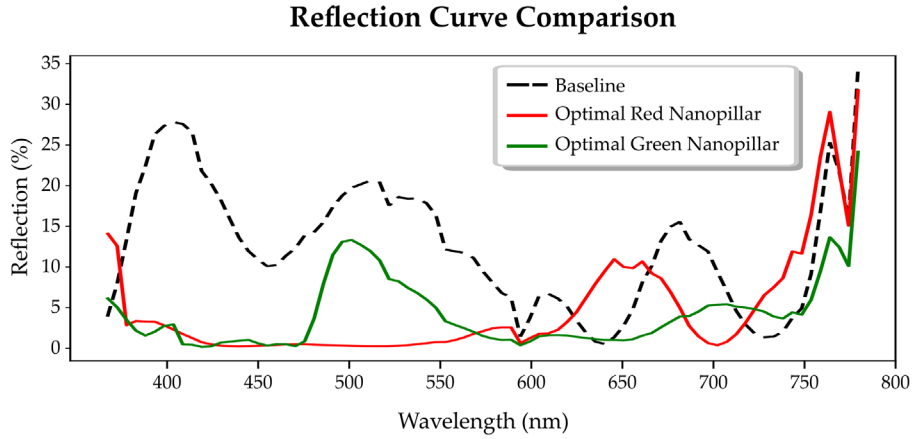

Figure 3.12 – Graphical comparison between of the percentual reflection curves for the optimal red and green nanopillar structures (in their respective colours) and the baseline structure (dashed) as defined in Table 3.

Figure 3.13 highlights the impact that the optimized nanopillars have on the simulated reflection curves. These data sets were achieved by re-simulating the optimized structures without their photonic structures so that only the optimal spiro and ITO values were preserved. Here it is shown that the anti-reflection effects these structures have are even more relevant when considering wavelengths outside the range of the desired colour. For instance, considering the green curves, the reflection curves differ particularly in the 400 to 500 nm range, where the monochromatic light would manifest purple or blue hues. This effect is especially noticeable when comparing the structured and unstructured red curves, where the red nanopillars reflect virtually no light in the green portion of the visible spectrum (the 500 to 600 nm range), opposed to reflection values of over 20% for the unstructured counterpart.

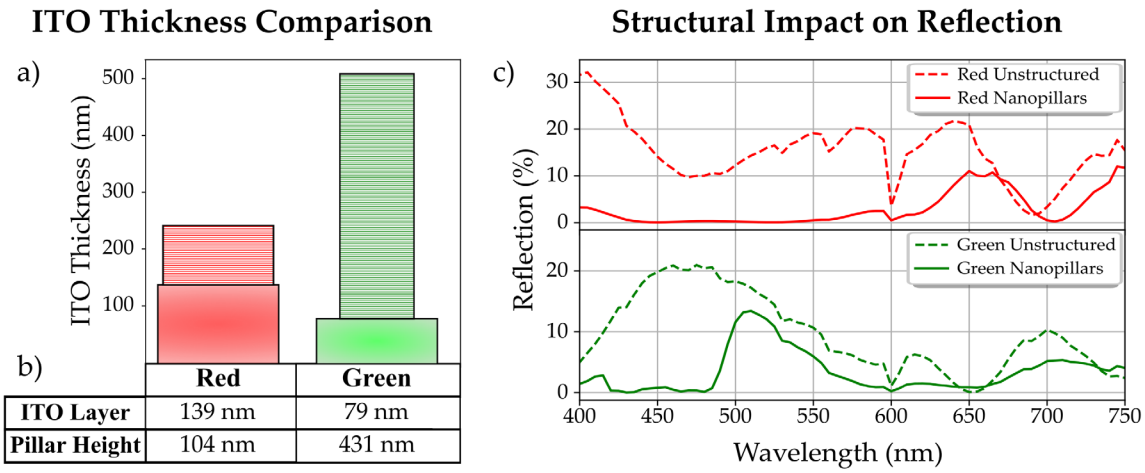

Figure 3.13 – ITO Thickness Comparison bar plot (a) and table (b) and Structural Impact on Reflection plots (c) for the red optimized nanopillars and green optimized nanopillars. The striped bars in the bar plot (a) represent the nanopillar structures, and their width is proportional to the optimal results.

4
CONCLUSION

This work aimed to establish an effective computational method for integration of colour into flexible photonic-enhanced solar cells. Though there is a proven demand for these technologies in the photovoltaic market, the concept remains novel and confined to theory, hence the need for simulation methods capable of maximizing this niche potential.

Summarily, the work hitherto described can be separated into four parts. To start, the author defined a method of quantifying colour proximity, the Colour Distance metric, hypothesized a set of FoMs with which to evaluate the performance of the PSCs, the Original and Root FoMs, and designed a practical albeit functional optimization process, the PSO method. Afterwards, a careful trial procedure was performed to tune the optimization algorithm, considering the data previously obtained from the planar sweeps to back up the initial optimization results. Sequentially, the Root FoM was selected as the standard measurement of performance, and the spiro layer thickness was excluded as a possible optimization variable, given the apparent weak correlation between it and the reflected colour. Finally, the variable optimization ranges were sieved twice over, once in an intermediate "Zoom PSO" and then once again to obtain the theoretical optimal parameters.

The final results are a culmination of over 150 individual optimization processes accumulated over thousands of computing hours. Ultimately, the results previously presented showed a remarkable increase in JSC upwards of 10.78% while also approximating the desired colour to a degree that would be indistinguishable to most human observers. These simulated optimal structures are capable of trapping incident light while simultaneously selectively interfering with any wavelength that would shift the hue of what little irradiance is reflected. This destructive interference is shown to be particularly prominent in the protruding geometrical features, which is verified when these structures exhibited colours that were initially absent from the preliminary planar sweeps, as was the case for the red nanopillars.

Regarding the optimization process, the predefined social and cognition indexes were deemed adequate, though oftentimes multiple optimizations had to be performed to ensure that the data was consistent and replicable despite the randomized PSO starting conditions.

Withal, these promising results hitherto presented may yet serve as the foundations upon which further optimizations can be developed.

Future Perspectives

In retrospect, the relevance of the colour distance values seems to drop off under a certain threshold number, dependent on the targetted colour and subjective perception. This could mean that a polynomial expression, defined by a diminishing weight for colour distance values of smaller than 30, might be better suited for the FoM. As is, the method seems to place too much emphasis on optimizing for minimal colour distance relative to JSC, a phenomenon that grows more disproportionate the closer the colour is to the intended value, which explains why the Root FoM outperformed the direct one-to-one Original FoM ratio.

Though the CIE 1931 XY method excelled in determining chromaticity, neglecting the lightness component of the reflected colour was but a simplification deemed necessary in these preliminary trials. For the sake of thoroughness, one might consider other, more elaborate methods of converting spectra into colour more comprehensively [74]. In any case, any alternative colour conversion methodology may be, in future pursuits, retrofitted into the already established PSO code base, contained in Appendix C. The Root FoM itself, while suitable for this purpose, should be subject to further testing and development.

In terms of the optimization process itself, there is still plenty of room for experimentation when considering other particle swarm topologies, specifically ring or star neighbourhood methods, that by restricting the flow of information across the swarm could optimize the earlier stages of exploitation by highlighting local maxima [59]. As the simulated volume size expanded, the optimization time also increased drastically before reaching a point where a single optimization, could take upwards of a week's worth of uninterrupted computing given the equipment provided. Ultimately, this meant that time constraints would ultimately render some of the more complex optimization processes unfeasible. To this end, alternative optimization functions, such as the Bayesian Method, could be a good fit for these resource-intensive optimizations, provided the parameter complexity is kept similarly limited [75], [76].

REFERENCES

[1] IEEFA, "Global solar demand to continue explosive growth in 2023—report | IEEFA." https://ieefa.org/articles/global-solar-demand-continue-explosive-growth-2023-report (accessed Mar. 16, 2023).

[2] "Global solar installations may hit 350.6 GW in 2023, says TrendForce – pv magazine International." https://www.pv-magazine.com/2023/02/16/global-solar-installations-may-hit-350-6-gw-in-2023-says-trendforce/ (accessed Mar. 16, 2023).

[3] Solar Power Europe, *Global Market Outlook For Solar Power/2022 - 2026*. 2022.

[4] A. Røyset, T. Kolås, and B. P. Jelle, "Coloured building integrated photovoltaics: Influence on energy efficiency," *Energy Build.*, vol. 208, p. 109623, Feb. 2020, doi: 10.1016/j.enbuild.2019.109623.

[5] European Commission, "European Commission Energy efficiency Energy Efficiency in Buildings," *Buildings*, no. March, pp. 16–17, 2011, Accessed: Sep. 22, 2022. [Online]. Available: https://ec.europa.eu/info/news/focus-energy-efficiency-buildings-2020-lut-17_en.

[6] A. Ghosh, S. Sundaram, and T. K. Mallick, "Colour properties and glazing factors evaluation of multicrystalline based semi-transparent Photovoltaic-vacuum glazing for BIPV application," *Renew. Energy*, vol. 131, pp. 730–736, 2019, doi: 10.1016/j.renene.2018.07.088.

[7] N. Martín-Chivelet *et al.*, "Building-Integrated Photovoltaic (BIPV) products and systems: A review of energy-related behavior," *Energy Build.*, vol. 262, 2022, doi: 10.1016/j.enbuild.2022.111998.

[8] H. Gholami and H. N. Røstvik, "Economic analysis of BIPV systems as a building envelope material for building skins in Europe," *Energy*, vol. 204, p. 117931, 2020, doi: 10.1016/j.energy.2020.117931.

[9] A. Roy, A. Ghosh, S. Bhandari, S. Sundaram, and T. K. Mallick, "Perovskite solar cells for bipv application: A review," *Buildings*, vol. 10, no. 7, pp. 1–33, 2020, doi: 10.3390/buildings10070129.

[10] M. Pelle, E. Lucchi, L. Maturi, A. Astigarraga, and F. Causone, "Coloured BIPV technologies: Methodological and experimental assessment for architecturally sensitive areas," *Energies*, vol. 13, no. 17, 2020, doi: 10.3390/en13174506.

[11] IEA-PVPS, "Report T15-07 - Coloured BIPV Market, Research and Development," 2019.

[12] T. E. Kuhn, C. Erban, M. Heinrich, J. Eisenlohr, F. Ensslen, and D. H. Neuhaus, "Review of technological design options for building integrated photovoltaics (BIPV)," *Energy Build.*, vol. 231, p. 110381, 2021, doi: 10.1016/j.enbuild.2020.110381.

[13] G. Yu, H. Yang, D. Luo, X. Cheng, and M. K. Ansah, "A review on developments and

researches of building integrated photovoltaic (BIPV) windows and shading blinds," *Renew. Sustain. Energy Rev.*, vol. 149, no. May, p. 111355, 2021, doi: 10.1016/j.rser.2021.111355.

[14] W. Zhang *et al.*, "Highly efficient perovskite solar cells with tunable structural color," *Nano Lett.*, vol. 15, no. 3, pp. 1698–1702, 2015, doi: 10.1021/nl504349z.

[15] M. M. Tavakoli *et al.*, "Highly Efficient Flexible Perovskite Solar Cells with Antireflection and Self-Cleaning Nanostructures," *ACS Nano*, vol. 9, no. 10, pp. 10287–10295, Oct. 2015, doi: 10.1021/acsnano.5b04284.

[16] P. Centeno *et al.*, "Self-Cleaned Photonic-Enhanced Solar Cells with Nanostructured Parylene-C," *Adv. Mater. Interfaces*, vol. 7, no. 15, p. 2000264, Aug. 2020, doi: 10.1002/admi.202000264.

[17] A. Ghosh, "Potential of building integrated and attached/applied photovoltaic (BIPV/BAPV) for adaptive less energy-hungry building's skin: A comprehensive review," *J. Clean. Prod.*, vol. 276, p. 123343, 2020, doi: 10.1016/j.jclepro.2020.123343.

[18] T. A. Hamed, A. Alshare, and H. El-Khalil, "Passive cooling of building-integrated photovoltaics in desert conditions: Experiment and modeling," *Energy*, vol. 170, pp. 131–138, Mar. 2019, doi: 10.1016/j.energy.2018.12.153.

[19] Z. Liu *et al.*, "A comprehensive study of feasibility and applicability of building integrated photovoltaic (BIPV) systems in regions with high solar irradiance," *J. Clean. Prod.*, vol. 307, no. April, p. 127240, 2021, doi: 10.1016/j.jclepro.2021.127240.

[20] A. Kojima, K. Teshima, Y. Shirai, and T. Miyasaka, "Organometal halide perovskites as visible-light sensitizers for photovoltaic cells," *J. Am. Chem. Soc.*, vol. 131, no. 17, pp. 6050–6051, May 2009, doi: 10.1021/ja809598r.

[21] A. S. Shikoh and A. Polyakov, "A Quantitative Analysis of the Research Trends in Perovskite Solar Cells in 2009–2019," *Phys. Status Solidi Appl. Mater. Sci.*, vol. 217, no. 23, 2020, doi: 10.1002/pssa.202000441.

[22] P. Roy, N. Kumar Sinha, S. Tiwari, and A. Khare, "A review on perovskite solar cells: Evolution of architecture, fabrication techniques, commercialization issues and status," *Sol. Energy*, vol. 198, no. December 2019, pp. 665–688, 2020, doi: 10.1016/j.solener.2020.01.080.

[23] J. Park *et al.*, "Controlled growth of perovskite layers with volatile alkylammonium chlorides," *Nat. 2023*, pp. 1–3, Feb. 2023, doi: 10.1038/s41586-023-05825-y.

[24] NREL, "Best Research-Cell Efficiency Chart. Photovoltaic Research. Accessed Mar. 2022," *https://www.nrel.gov/pv/cell-efficiency.html*, 2021. https://www.nrel.gov/pv/cell-efficiency.html (accessed Mar. 16, 2023).

[25] N. Li, X. Niu, Q. Chen, and H. Zhou, "Towards commercialization: The operational stability of perovskite solar cells," *Chem. Soc. Rev.*, vol. 49, no. 22, pp. 8235–8286, 2020, doi: 10.1039/d0cs00573h.

[26] F. Enrichi and G. C. Righini, "Solar cells and light management: Materials, strategies and sustainability," *Sol. Cells Light Manag. Mater. Strateg. Sustain.*, pp. 1–556, 2019, doi: 10.1016/C2017-0-04229-5.

[27] T. Wu *et al.*, "The Main Progress of Perovskite Solar Cells in 2020–2021," *Nano-Micro Lett.*, vol. 13, no. 1, 2021, doi: 10.1007/s40820-021-00672-w.

[28] J. P. Correa-Baena *et al.*, "Promises and challenges of perovskite solar cells," *Science (80-*

.)., vol. 358, no. 6364, pp. 739–744, 2017, doi: 10.1126/science.aam6323.
[29] C. C. Boyd, R. Cheacharoen, T. Leijtens, and M. D. McGehee, "Understanding Degradation Mechanisms and Improving Stability of Perovskite Photovoltaics," *Chem. Rev.*, vol. 119, no. 5, pp. 3418–3451, 2019, doi: 10.1021/acs.chemrev.8b00336.
[30] Q. Wang, N. Phung, D. Di Girolamo, P. Vivo, and A. Abate, "Enhancement in lifespan of halide perovskite solar cells," *Energy Environ. Sci.*, vol. 12, no. 3, pp. 865–886, 2019, doi: 10.1039/C8EE02852D.
[31] L. Qiu, L. K. Ono, and Y. Qi, "Advances and challenges to the commercialization of organic–inorganic halide perovskite solar cell technology," *Mater. Today Energy*, vol. 7, pp. 169–189, Mar. 2018, doi: 10.1016/j.mtener.2017.09.008.
[32] X. Zhao *et al.*, "Accelerated aging of all-inorganic, interface-stabilized perovskite solar cells," *Science (80-.).*, vol. 377, no. 6603, pp. 307–310, Jul. 2022, doi: 10.1126/SCIENCE.ABN5679/SUPPL_FILE/SCIENCE.ABN5679_SM.PDF.
[33] D. C. Jordan and S. R. Kurtz, "Photovoltaic Degradation Rates-an Analytical Review," *Prog. Photovoltaics Res. Appl.*, vol. 21, no. 1, pp. 12–29, Jan. 2013, doi: 10.1002/pip.1182.
[34] S. Haque, M. J. Mendes, O. Sanchez-Sobrado, H. Águas, E. Fortunato, and R. Martins, "Photonic-structured TiO 2 for high-efficiency, flexible and stable Perovskite solar cells," *Nano Energy*, vol. 59, no. January, pp. 91–101, 2019, doi: 10.1016/j.nanoen.2019.02.023.
[35] K. Li *et al.*, "Light trapping in solar cells: simple design rules to maximize absorption," *Optica*, vol. 7, no. 10, p. 1377, 2020, doi: 10.1364/optica.394885.
[36] M. L. Brongersma, Y. Cui, and S. Fan, "Light management for photovoltaics using high-index nanostructures," *Nat. Mater.*, vol. 13, no. 5, pp. 451–460, 2014, doi: 10.1038/nmat3921.
[37] J. Grandidier, M. G. Deceglie, D. M. Callahan, and H. A. Atwater, "Simulations of solar cell absorption enhancement using resonant modes of a nanosphere array," *Physics, Simulation, Photonic Eng. Photovolt. Devices*, vol. 8256, p. 825603, 2012, doi: 10.1117/12.909677.
[38] A. Lennon, M. Lunardi, B. Hallam, and P. R. Dias, "The aluminium demand risk of terawatt photovoltaics for net zero emissions by 2050," *Nat. Sustain.*, Jan. 2022, doi: 10.1038/s41893-021-00838-9.
[39] P. Sadorsky, "Forecasting solar stock prices using tree-based machine learning classification: How important are silver prices?," *North Am. J. Econ. Financ.*, vol. 61, p. 101705, Jul. 2022, doi: 10.1016/j.najef.2022.101705.
[40] M. J. Mendes *et al.*, "Design of optimized wave-optical spheroidal nanostructures for photonic-enhanced solar cells," *Nano Energy*, vol. 26, pp. 286–296, 2016, doi: 10.1016/j.nanoen.2016.05.038.
[41] M. J. Mendes *et al.*, "Optimal-Enhanced Solar Cell Ultra-thinning with Broadband Nanophotonic Light Capture," *iScience*, vol. 3, pp. 238–254, 2018, doi: 10.1016/j.isci.2018.04.018.
[42] C. S. Schuster *et al.*, *Empowering Photovoltaics with Smart Light Management Technologies*. 2021.
[43] O. Isabella, R. Vismara, D. N. P. Linssen, K. X. Wang, S. Fan, and M. Zeman, "Advanced light trapping scheme in decoupled front and rear textured thin-film silicon solar cells,"

Sol. Energy, vol. 162, no. October 2017, pp. 344–356, 2018, doi: 10.1016/j.solener.2018.01.040.

[44] V. E. Ferry, A. Polman, and H. A. Atwater, "Modeling Light Trapping in Nanostructured Solar Cells," *ACS Nano*, vol. 5, no. 12, pp. 10055–10064, Dec. 2011, doi: 10.1021/nn203906t.

[45] Z. Xu *et al.*, "Role of nanocone and nanohemisphere arrays in improving light trapping of thin film solar cells," *Opt. Commun.*, vol. 377, pp. 104–109, Oct. 2016, doi: 10.1016/j.optcom.2016.05.050.

[46] S. Haque, M. Alexandre, M. J. Mendes, H. Águas, E. Fortunato, and R. Martins, "Design of wave-optical structured substrates for ultra-thin perovskite solar cells," *Appl. Mater. Today*, vol. 20, p. 100720, 2020, doi: 10.1016/j.apmt.2020.100720.

[47] J. Grandidier *et al.*, "Solar cell efficiency enhancement via light trapping in printable resonant dielectric nanosphere arrays," *Phys. Status Solidi Appl. Mater. Sci.*, vol. 210, no. 2, pp. 255–260, 2013, doi: 10.1002/pssa.201228690.

[48] A. Taflove and S. C. Hagness, *The Finite-Difference Time-Domain Method Third Edition*. 2005.

[49] Kane Yee, "Numerical solution of initial boundary value problems involving maxwell's equations in isotropic media," *IEEE Trans. Antennas Propag.*, vol. 14, no. 3, pp. 302–307, May 1966, doi: 10.1109/TAP.1966.1138693.

[50] G. V. G. Baranoski, "An Overview of Light , Optics and Appearance Concepts Light as Radiation," pp. 1–20, 2008.

[51] A. K. Roy Choudhury, *Visual measures of colour*, vol. 2. 2015.

[52] A. D. Broadbent, "A critical review of the development of the CIE1931 RGB color-matching functions," *Color Res. Appl.*, vol. 29, no. 4, pp. 267–272, 2004, doi: 10.1002/col.20020.

[53] J. Schanda, *Colorimetry: Understanding the CIE System*. Wiley, 2007.

[54] E. Reinhard, E. A. Khan, A. Oğuz Akyüz, and G. Johnson, *Color imaging: Fundamentals and applications*. 2008.

[55] H. Lee and H. J. Song, "Current status and perspective of colored photovoltaic modules," *Wiley Interdiscip. Rev. Energy Environ.*, vol. 10, no. 6, pp. 1–31, 2021, doi: 10.1002/wene.403.

[56] W. Burger and M. J. Burge, *Principles of Digital Image Processing*. London: Springer London, 2009.

[57] I. E. Society, "Table T-5B: Color-Matching Functions and Chromaticity Coordinates of CIE 1964 Supplementary Standard Colorimetric Observer – Illuminating Engineering Society." [Online]. Available: https://www.ies.org/definitions/table-t-5b-color-matching-functions-and-chromaticity-coordinates-of-cie-1964-supplementary-standard-colorimetric-observer/.

[58] W. D. Wright, "A re-determination of the trichromatic coefficients of the spectral colours," *Trans. Opt. Soc.*, vol. 30, no. 4, p. 141, Mar. 1929, doi: 10.1088/1475-4878/30/4/301.

[59] K. E. Parsopoulos and M. N. Vrahatis, *Particle Swarm Optimization and Intelligence*, vol. 270. 2010.

[60] M. G. Sahab, V. V. Toropov, and A. H. Gandomi, *A Review on Traditional and Modern*

Structural Optimization: Problems and Techniques, First Edit. Elsevier Inc., 2013.
[61] K. M. Ting, *Encyclopedia of Machine Learning*. Boston, MA: Springer US, 2010.
[62] J. G. Mutitu *et al.*, "Thin film solar cell design based on photonic crystal and diffractive grating structures," *Opt. Express*, vol. 16, no. 19, p. 15238, Sep. 2008, doi: 10.1364/OE.16.015238.
[63] L. Zagaglia, V. Demontis, F. Rossella, and F. Floris, "Particle swarm optimization of GaAs-AlGaAS nanowire photonic crystals as two-dimensional diffraction gratings for light trapping," *Nano Express*, vol. 3, no. 2, p. 021001, Jun. 2022, doi: 10.1088/2632-959X/ac61ec.
[64] X.-S. Yang, "Particle Swarm Optimization," in *Nature-Inspired Optimization Algorithms*, Elsevier, 2014, pp. 99–110.
[65] M. J. Mendes *et al.*, "Wave-optical front structures on silicon and perovskite thin-film solar cells," *Sol. Cells Light Manag. Mater. Strateg. Sustain.*, pp. 315–354, Jan. 2020, doi: 10.1016/B978-0-08-102762-2.00009-4.
[66] E. Unger and T. J. Jacobsson, "The Perovskite Database Project: A Perspective on Collective Data Sharing," *ACS Energy Lett.*, vol. 7, no. 3, pp. 1240–1245, Mar. 2022, doi: 10.1021/acsenergylett.2c00330.
[67] T. A. F. König *et al.*, "Electrically Tunable Plasmonic Behavior of Nanocube–Polymer Nanomaterials Induced by a Redox-Active Electrochromic Polymer," *ACS Nano*, vol. 8, no. 6, pp. 6182–6192, Jun. 2014, doi: 10.1021/nn501601e.
[68] T. Siefke *et al.*, "Materials Pushing the Application Limits of Wire Grid Polarizers further into the Deep Ultraviolet Spectral Range," *Adv. Opt. Mater.*, vol. 4, no. 11, pp. 1780–1786, Nov. 2016, doi: 10.1002/adom.201600250.
[69] M. van Eerden *et al.*, "Optical Analysis of Planar Multicrystalline Perovskite Solar Cells," *Adv. Opt. Mater.*, vol. 5, no. 18, p. 1700151, Sep. 2017, doi: 10.1002/adom.201700151.
[70] M. Filipič *et al.*, "CH_3NH_3PbI_3 perovskite / silicon tandem solar cells: characterization based optical simulations," *Opt. Express*, vol. 23, no. 7, p. A263, Apr. 2015, doi: 10.1364/OE.23.00A263.
[71] E. D. Palik, "Handbook of Optical Constants of Solids.," p. 1117, 1991.
[72] J. Robinson and Y. Rahmat-Samii, "Particle swarm optimization in electromagnetics," *IEEE Trans. Antennas Propag.*, vol. 52, no. 2, pp. 397–407, 2004, doi: 10.1109/TAP.2004.823969.
[73] C. Sammut and G. I. Webb, *Encyclopedia of Machine Learning*. Boston, MA: Springer US, 2010.
[74] T. Mansencal *et al.*, "Colour 0.4.2," Nov. 2022, doi: 10.5281/ZENODO.7367239.
[75] L. Tani and C. Veelken, "Comparison of Bayesian and particle swarm algorithms for hyperparameter optimisation in machine learning applications in high energy physics," Jan. 2022, [Online]. Available: http://arxiv.org/abs/2201.06809.
[76] J. Maryak, J. Mockus, W. Eddy, A. Mockus, L. Mockus, and G. Reklaitis, "Bayesian Heuristic Approach to Discrete and Global Optimization," *Technometrics*, vol. 41, no. 4, p. 378, Nov. 1999, doi: 10.2307/1271369.
[77] J. Lourenço, "NOVAThesis Template," 2022. https://github.com/joaomlourenco/novathesis_word.

Appendix A: Material Data

The material data regarding real and imaginary part refractive indexes employed in the simulations hitherto described is plotted in Figure A.1.

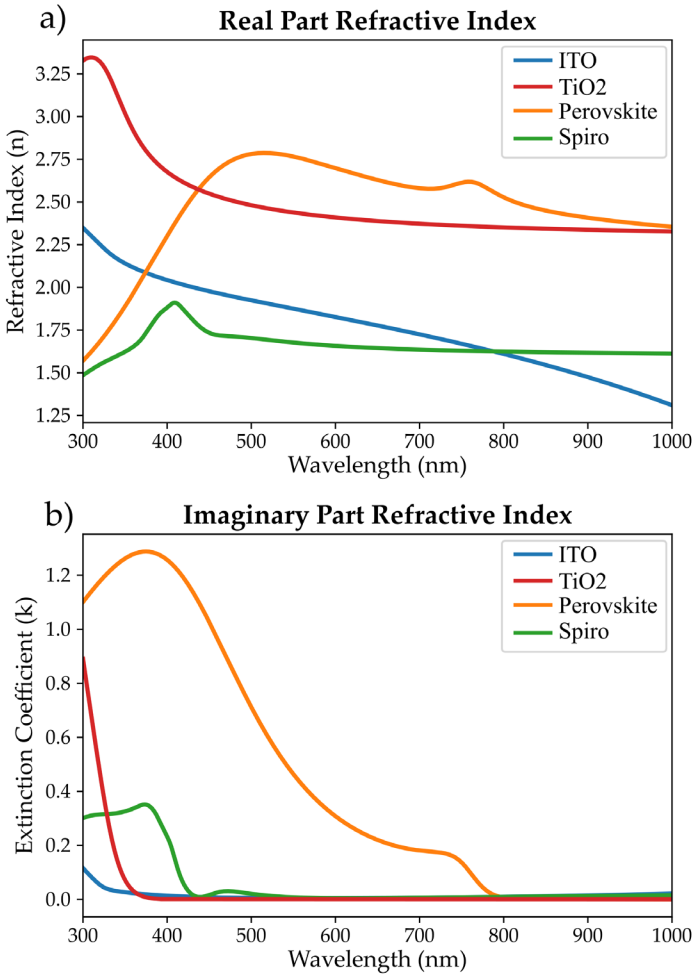

Figure A.1 – Real (a) and Imaginary (b) Part Refractive index plots for ITO, TiO2, Perovskite and Spiro, sourced from Konig et. al [67], Siefke et. al [68], van Eerden et. al [69], and Filipič et. al [70] respectively.

The material data shown in Figure A.1 was obtained through polynomial regression of experimental datasets, the tolerances, coefficients, and root-mean-squared errors of which are summarized in Table A.1.

Table A.1 – Table summarizing the data fitting parameters for Ag, Spiro, Perovskite, TiO_2, and ITO and the ensuing standard and weighted root-mean-squared errors.

	Ag	Spiro	Perovskite	TiO2	ITO
Fit Tolerance	0.0004	0.001	0.1	0.01	0.0001
Maximum Coefficient	12	12	6	5	12
Number of Coefficients	9	11	6	5	6
Standard RMS error	2.36E-01	1.74E-02	4.00E-02	3.59E-02	1.29E-02
Weighted RMS error	4.21E-02	8.69E-03	4.00E-02	3.94E-03	7.16E-03

Appendix B:
SIMULATION SETTINGS

This appendix summarizes the simulation settings used in Table B.1.

Table B.1 – Summary of the most relevant Ansys Lumerical FDTD simulation settings used.

Source Settings*	
Minimum Wavelength	300 nm
Maximum Wavelength	1000 nm
Frequency Points	100
Solar Gen Settings	
Down Sample X	3
Down Sample Y	3
Down Sample Z	2
FDTD Settings	
Simulation Time	750 fs
Simulation Temperature	300 K
Background Material Index	1
Mesh Accuracy**	3
Auto Shutoff Minimum	1.00E-05
Boundary Conditions	
X min	Anti-Symmetric
X max	Anti-Symmetric
Y min	Symmetric
Y max	Symmetric
Z max	Metal
Z max	PML
PML Layers	32

(*) The reflection monitors used to calculate colour consider an array of wavelengths from 380 nm to 780 nm divided in 81 equally spaced intervals of 5 nm.

(**) Mesh refinements with index equivalent to 5 were applied in all dimensions from the top of the structures down to 200 nm underneath the top of the perovskite absorber layer.

Appendix C:
PARTICLE SWARM CODE

The final version of the PSO python script, used for the obtention of the results presented in Chapter 3.7 is as follows:

```
"""
Implementation of the particle swarm optimization algorithm
"""
import logging
from logging.config import fileConfig
import os
from random import random
from typing import Dict, List, Tuple
import matplotlib.pyplot as plt
import numpy as np
import numpy.typing as npt
import pandas as pd

def _update_parameters(
    param, vel, max_param, min_param, inertia_w, ind_cog, soc_learning,
pbest, gbest
):
    """
    Update equation for the particle swarm algorithm
    V_ij^(t+1) =
        learning rate : w*V_ij^t
        cognitive part : c1*r1*(pbest_ij - p_ij^t)
        social part : c2*r2*(gbest_ij - p_ij^t)
    Args:
        param - input variables (ij array - i particles, i parameters)
        vel - input velocities (ij array)
        max_param - maximum parameter values
        min_param - minimum parameter values
        inertia_w - inertia weight constant
        ind_cog - individual cognition parameter
        soc_learning - social learning parameter
        pbest - best set of parameters for a certain particle (ij array)
        gbest - best global set of parameters (i array)
    Return:
        Updated parameters and velocities
    """
    logging.debug("Update Properties --------------")
    logging.debug("Initialization -----------")
    logging.debug(f"Init values: {inertia_w}, {ind_cog}, {soc_learning}")
    logging.debug(f"vel=\n{vel}")
```

```
        logging.debug(f"pbest=\n{pbest}")
        logging.debug(f"gbest=\n{gbest}")
        r1 = random()
        r2 = random()
        max_param = np.broadcast_to(max_param[:, np.newaxis], param.shape)
        min_param = np.broadcast_to(min_param[:, np.newaxis], param.shape)
        logging.debug(f"min_param:\n{min_param}")
        logging.debug(f"max_param:\n{max_param}")
        logging.debug("Calculations -----------")
        # Update velocity
        part_1 = inertia_w * vel
        part_2 = ind_cog * r1 * (pbest - param)
        part_3 = soc_learning * r2 * (gbest - param)
        v_new = part_1 + part_2 + part_3
        logging.debug(f"v_new:\n{v_new}")
        # Check if no parameters are outside the allowed ranges for the
    parameters
        logging.debug(f"param=\n{param}")
        param_new = param + v_new
        logging.debug(f"param_new:\n{param_new}")
        mask_min = param_new < min_param
        mask_max = param_new > max_param
        logging.debug(f"mask_min:\n{mask_min}")
        logging.debug(f"mask_max:\n{mask_max}")
        param_new[mask_min] = min_param[mask_min]
        param_new[mask_max] = max_param[mask_max]
        logging.debug(f"Parameter Space:\n{param_new}")
        v_new[mask_min & mask_max] = 0
        logging.debug(f"Velocity space:\n{v_new}")
        return param_new, v_new

    def particle_swarm(
        func,
        param_dict: Dict[str, List[float]],
        *,
        maximize: bool = True,
        inert_prop: Tuple[float, float, bool] = (0.9, 0.4, True),
        ind_cog: float = 1.45,
        soc_learning: float = 1.45,
        particles: int = 25,
        iterations: Tuple[int, int, bool] = (50, 100, True),
        tolerance: Tuple[float, int] = (0.05, 10),
        progress: bool = True,
        export: bool = False,
        basepath: str = "PSO_Results",
        **func_kwargs,
    ):
        """Implementation of the particle swarm algorithm
        Args:
            - func: optimization function
            - param_dict: dictionary with parameters and variation range
            - maximize: maximize or minimize the problem (default: maximize)
            - inert_prop: Inertial weight factor (start value, finish value,
            static/dynamic)
            - ind_cog: cognition index for particles (default = 1.45)
            - soc_learning: social learning index (default = 1.45)
            - particles: Number of particles (default: 25)
            - iteration: Define number of iterations (min, max, static/dynamic)
```

```
        - max_iterations: Max number of iterations (default = 100)
        - tolerance_percent
        - export: Export files with PSO data
        - basepath: Base path to save export and progress information
        - func_kwargs: Extra arguments to pass to the optimization function
    Return:
        - gfitness: Best value obtained
        - gbest: Best parameters
        - pbest: Best parameters for each particle
        - gbest_array: Array with the gfitness value for each iteration
    """
    # Create export path
    if export and not os.path.isdir(basepath):
        logging.info(f"Creating {basepath=}...")
        os.mkdir(basepath)
    min_iteration, max_iteration, iteration_check = iterations
    if max_iteration < min_iteration:
        raise Exception("max_iteration must be bigger than min_iteration")
    if not iteration_check:
        max_iteration = min_iteration
    # Create an array for the inertial factor variation (its max_iteration
size)
    inert_factor_low, inert_factor_up, inert_sweep = inert_prop
    if inert_sweep:
        inert_factor = np.linspace(inert_factor_low, inert_factor_up,
min_iteration)
        inert_factor_remaining = np.array(
            [inert_factor_up] * (max_iteration - min_iteration)
        )
        inert_factor = np.r_[inert_factor, inert_factor_remaining]
    else:
        inert_factor = np.ones(max_iteration) * inert_factor_up
    logging.info(f"Inert_factor array:\n{inert_factor}")
    # Variable initialization
    param_names = list(param_dict.keys())
    vparam_names = [f"v{param_name_i}" for param_name_i in param_names]
    export_names = param_names.copy()
    export_names.append("FoM")
    export_names.extend(vparam_names)
    logging.debug(f"Parameters in study:\n{export_names}")
    param_max = np.array([p_max[1] for p_max in param_dict.values()])
    param_min = np.array([p_min[0] for p_min in param_dict.values()])
    # Random array with the start value for the parameters
    param_space = [
        np.random.uniform(param_dict[param][0], param_dict[param][1],
size=(particles))
        for param in param_names
    ]
    param_space = np.stack(param_space)
    # Random array with the start value for the velocities
    vel_space = [
        np.random.uniform(
            -np.abs(max(param_dict[param]) - min(param_dict[param])),
            np.abs(max(param_dict[param]) - min(param_dict[param])),
            size=(particles),
        )
        for param in param_names
    ]
```

```
157         vel_space = np.stack(vel_space)
158         # First run of the PSO outside loop
159         iteration = 1
160         func_input = {
161             param_name: param_space[i] for i, param_name in
162     enumerate(param_names)
163         }
164         func_results = func(**func_input, **func_kwargs)
165         if maximize:
166             fitness_arg = np.argmax(func_results)
167         else:
168             fitness_arg = np.argmin(func_results)
169         # PSO optimization arrays (gfitness, pfitness, gbest, pbest, tol_array)
170         tolerance_percent, tolerance_num = tolerance
171         gfitness = func_results[fitness_arg]
172         pfitness = func_results
173         gbest = param_space[:, fitness_arg].flatten()
174         tol_array = [0]
175         gbest_array = [gfitness]
176         pbest = param_space
177         # Create figure handler to show the results
178         if progress:
179             _, ax = plt.subplots(
180                 1,
181                 2,
182                 figsize=(5, 4),
183                 gridspec_kw={"wspace": 0.1, "width_ratios": [0.7, 0.3]},
184             )
185             logging.debug(f"{np.arange(iteration)}::{gbest_array}")
186             _preview_results(
187                 ax, np.arange(iteration), gbest_array, pbest[:, -1],
188     param_names
189             )
190         # Export data
191         if export:
192             export_data = np.c_[param_space.T, func_results, vel_space.T]
193             export_df = pd.DataFrame(export_data, columns=export_names)
194             export_df.to_csv(
195                 os.path.join(basepath, f"pso_it{iteration:03d}.csv"), sep=" ",
196     index=False
197             )
198         while iteration < max_iteration:
199             # Check for the tolerance condition on the last tol_num values of
200     the tolerance array
201             if iteration > min_iteration + tolerance_num:
202                 last_tolerances = np.array(tol_array)[-tolerance_num:]
203                 logging.debug(f"tol_array: {tol_array}\n{len(tol_array)}")
204                 logging.debug(f"last_tolerances:
205     {last_tolerances}\n{len(last_tolerances)}")
206                 avg_tol = np.average(last_tolerances)
207                 logging.debug(f"avg_tol: {avg_tol}")
208                 if avg_tol < tolerance_percent:
209                     logging.warn(f"Tolerance reached at {iteration}...
210     Exiting")
211                     break
212             logging.info(f"PSO Running Iteration: {iteration}")
213             param_space, vel_space = _update_parameters(
214                 param_space,
```

```
            vel_space,
            param_max,
            param_min,
            inert_factor[iteration - 1],
            ind_cog,
            soc_learning,
            pbest,
            gbest[:, np.newaxis],
        )
        # Update gbest and pbest
        func_input = {
            param_name: param_space[i] for i, param_name in
enumerate(param_names)
        }
        func_results = func(**func_input, **func_kwargs)
        gfitness_old = gfitness
        if maximize:
            fitness_candidate_ind = np.argmax(func_results)
            if func_results[fitness_candidate_ind] > gfitness:
                gfitness = func_results[fitness_candidate_ind]
                gbest = param_space[:, fitness_candidate_ind].flatten()
            pfitness_mask = func_results > pfitness
        else:
            fitness_candidate_ind = np.argmin(func_results)
            if func_results[fitness_candidate_ind] < gfitness:
                gfitness = func_results[fitness_candidate_ind]
                gbest = param_space[:, fitness_candidate_ind].flatten()
            pfitness_mask = func_results < pfitness
        # Add error values to array
        tol_array.append((gfitness - gfitness_old) / gfitness_old)
        # Update gbest, pfitness and pbest
        logging.debug(f"Global best list:\n{gbest}")
        gbest_array.append(gfitness)
        # Update the FoM plot
        pfitness[pfitness_mask] = func_results[pfitness_mask]
        pbest[:, pfitness_mask] = param_space[:, pfitness_mask]
        logging.debug(f"Particle Best Values:\n{pfitness}")
        logging.debug(f"Particle Global best list:\n{pbest}")
        iteration += 1
        if progress:
            _preview_results(
                ax, np.arange(iteration), gbest_array, pbest[:, -1],
param_names
            )
        if export:
            export_data = np.c_[param_space.T, func_results, vel_space.T]
            export_df = pd.DataFrame(export_data, columns=export_names)
            export_df.to_csv(
                os.path.join(basepath, f"pso_it{iteration:03d}.csv"),
                sep=" ",
                index=False,
            )
    logging.debug(

f"Results:\ngfitness:{gfitness}\ngbest:\n{gbest}\npbest:\n{pbest}\ngbest_ar
ray:\n{gbest_array}"
    )
    return gfitness, gbest, pbest, gbest_array
```